Circulation dynamics and cross-shelf transport mechanisms in the Florida Big Bend

By

Austin C. Todd, Steven L. Morey, and Eric P. Chassignet

Austin C. Todd
Department of Marine, Earth and Atmospheric Sciences
North Carolina State University, Raleigh, NC, 27695
Email: actodd@ncsu.edu

Steven L. Morey
Center for Ocean-Atmospheric Prediction Studies
The Florida State University
Tallahassee, FL 32306-2840
Email: smorey@fsu.edu

Eric P. Chassignet
Center for Ocean-Atmospheric Prediction Studies
The Florida State University
Tallahassee, FL 32306-2840
Email: echassignet@fsu.edu

ABSTRACT

The Florida Big Bend region in the northeastern Gulf of Mexico contains both spawning sites and nursery habitats for a variety of economically valuable marine species. One species, the gag grouper (Mycteroperca microlepis), relies on the shelf circulation to distribute larvae from shelf-break spawning grounds to coastal seagrass nurseries each spring. Therefore, identifying the dominant circulation features and physical mechanisms that contribute to cross-shore transport during the springtime is a necessary step in understanding the variation of the abundance of this reef fish. In this paper, an examination of the physical mechanisms by which cross-shelf movement is possible, and the pathways by which materials may be transported onshore are presented. The role of variable wind stress and conservation of potential vorticity in setting the net across-shelf transport are investigated using a very high horizontal resolution (800—900 m) numerical ocean model. Four contemporaneous simulations are run by forcing the ocean model with four different atmospheric products over the period 2004-2010, and are evaluated on the basis of their ability to accurately represent the mean flow features in the region. The simulations demonstrate that the springtime shelf circulation responds primarily to large-scale, low frequency wind stress, the mean circulation patterns are set by the rectification of flow during northwesterly or southeasterly-directed wind stress, and significant cross-shelf flow may be generated during winds from the northwest. The springtime flow is mostly barotropic and tends to conserve potential vorticity over time scales shorter than about 12 hours. For longer time scales, the nonconservation of potential vorticity enables movement of particles inshore. Particle advection experiments demonstrate that a primary pathway exists south of St. George Island by which particles are able to reach inshore, and that preferred release locations for particles to successfully arrive inshore coincide with a known gag spawning aggregation site. The results

provide, for the first time, a description of the mechanisms by which onshore transport is possible from gag spawning sites at the shelf break to seagrass nurseries at the coast.

1. Introduction

The Florida Big Bend region (BBR) in the northeastern Gulf of Mexico (NEGOM) is located at the juncture of the Florida Peninsula and the Florida Panhandle, where the coastline orientation changes by roughly 90 degrees. The seagrass meadows along the coastline and the numerous reefs across the BBR provide both nursery habitats and spawning sites for a variety of marine species. The ecologically diverse and economically productive marine ecosystems of the BBR have been studied for fisheries production (i.e., Hood and Schlieder, 1992; Koenig and Coleman, 1998; Koenig *et al*., 2000; Gentner, 2009). The physical oceanographic state can affect reef fish development by setting egg and larval dispersion patterns and by influencing locations containing available food (Rothschild and Osborn, 1988; Werner *et al*., 1997). Ocean currents have been surmised to be the dominant mechanism responsible for the horizontal dispersion of fertilized eggs and planktonic larvae (Norcross and Shaw, 1984). Ocean currents can also affect the distribution of food sources in the region, which mostly come from the nutrient-laden, high-chlorophyll coastal waters or via nutrient fluxes from the deep-ocean (He and Weisberg, 2003). Therefore, the shelf circulation can directly influence the recruitment and year-class strength of given species by moving fish eggs and larvae to or from areas that are conducive for survival (Norcross and Shaw, 1984).

The ocean's circulation on continental shelves is driven by a combination of local surface forcing, tides, rivers, and deep-ocean fluxes near the shelf break. However, the dominant forcing mechanism on the West Florida Shelf (WFS) and Florida Panhandle Shelf is the wind-driven component of this forcing, as the NEGOM shelf circulation has a strong relationship with the local wind stress (Mitchum and Clarke, 1986; Morey and O'Brien, 2002; Morey *et al*., 2005; Weisberg *et al*., 2005). From late fall through the spring, the winds over the BBR are dominated by synoptic events associated with the passage of cold fronts. The strength, duration, and frequency of these frontal winds vary interannually, when some years have stronger or more frequent frontal passages. The differences in shelf circulation patterns and the amount of upwelling from year to year can be largely attributed to the interannual differences in the strength and duration of upwelling-favorable wind events (Weisberg and He, 2003).

Understanding the impact of oceanic transport on reef fish recruitment is crucial for effective fisheries management (Fitzhugh *et al*., 2005). Commercial and recreational fishing cause reductions in both adult fish abundance and juvenile fish populations in the Gulf of Mexico (GOM), and recreational fishing accounts for over 60% of annual landings of certain fish species (Coleman *et al*., 2004). Although fishing pressures can affect population size, population-independent processes that occur during their egg, larval, and early juvenile stages are significant in determining the interannual variability in fish recruitment (Rothschild, 1986; Chambers and Trippel, 1997). Among these processes is the transport of eggs, larvae, and early juveniles by the ocean currents.

The gag grouper (*Mycteroperca microlepis*) relies on the circulation for transport of its eggs and larvae during the pelagic stage of its early life cycle (Keener *et al*., 1988; Fitzhugh *et al*., 2005; Koenig and Coleman, 1998). Gag are among the most valuable finfish in the region, recently estimated to provide over $100 million in value added and over $60 million in income to the southeastern United States from recreational fishing alone (Gentner, 2009). Adult gag form spawning aggregations along offshore reefs near the continental shelf break (50—100 m depth) from January–April, with peak spawning in February and March (Hood and Schlieder, 1992; Coleman *et al*., 1996; Koenig *et al*., 2000; Fitzhugh *et al*., 2005). Their larvae spend 30–60 days (mean ~43 days) in the water column before settlement in the coastal seagrasses some 70–600 km away (a period known as their pelagic larval duration) (Koenig and Coleman, 1998; Fitzhugh *et al*., 2005). The vertical positions of gag larvae in the water column and their behavior during this stage of development are not fully understood. Keener *et al*. (1988) found evidence of a diel vertical migration in conjunction with tidal phase near barrier island inlets in South Carolina. However, while tides might play a more pronounced role in the nearshore environment of their study region, tidal amplitudes and tidal residual currents over the BBR shelf remain small (He and Weisberg, 2002a; Gouillon *et al*., 2010). In addition, estimating the onshore transport mechanisms for gag larvae in the BBR using an empirical model based on surface drifters and winds by Fitzhugh *et al*. (2005) proved to be unsuccessful. They suggested that a fully three-dimensional approach is needed in order to understand the physical transport processes in the region.

Studies in the BBR have included short-lived observations (i.e., Marmorino, 1983a,b; Weatherly and Thistle, 1997), single-station time series (i.e. Weatherly and Thistle, 1997; Maksimova and Clarke, 2013), or those focused on general dynamics of the WFS (Mitchum and Sturges, 1982; Mitchum and Clarke, 1986; Weisberg and He, 2003; Weisberg *et al*., 2005; Yang and Weisberg, 1999). However, with such a unique bathymetry in the BBR, one cannot simply apply theory applicable to a long wide shelf such as the southern part of the WFS to the region. The BBR undergoes a dramatic transition from the very wide WFS (150—200 km wide) to the very narrow Florida Panhandle Shelf (40 km at its narrowest point). This transition occurs offshore of Cape San Blas and Cape St. George, where the isobaths converge and undergo tight curvature (Fig. 1). The observational studies in the region have indicated that the change in coastline orientation in the BBR makes it a dynamically ineresting area, since there does not exist a clear relationship between the alongshore current and the wind stress here (Marmorino, 1983a). The bathymetric features of the region play an important role in setting the circulation and transport.

Previous observational studies (Marmorino, 1983a,b; Weatherly and Thistle, 1997; Mitchum and Clarke, 1986) consent that the NEGOM shelf waters are in dominant balance with the local wind stress, so the ocean should be expected to have a different response to changes of the surface atmospheric representation. To better understand the sensitivity of the circulation in this region to changes in surface forcing, this study uses a numerical ocean model forced by four data-assimilative atmospheric models, each with a different set of grid spacings, output frequencies, and physics. The four-dimensional, high-resolution numerical modeling approach also provides a tool to understand the general dynamics governing the BBR circulation and the transport during the spring months.

The coastal circulation is found to respond barotropically to large-scale, low-frequency variations in the wind stress in conjunction with atmospheric frontal passages, which generate oscillations between phases of southeasterly and northwesterly-directed wind stress. The shelf circulation responds asymmetrically to the oscillating winds, resulting in a rectification of the flow with mean currents that are directed across-shelf in the area offshore Cape San Blas and Cape St. George. The flow tends to conserve potential vorticity on time scales less than 12 hours, but over longer time scales the nonconservation of potential vorticity enhances the ability for onshore movement. The primary pathway for onshore transport exists to the southeast of Cape St. George, and a preferred origin for materials to successfully arrive inshore coincides with a known gag spawning aggregation.

The information is presented in this manuscript as follows: The ocean model that is used as the primary tool for understanding the ocean circulation is described in section 2. In section 3, the ocean model simulations are compared to a suite of regional observations, and the mean circulation features are described along with their variability. Section 4 provides a description the physical mechanisms by which cross-shelf transport is possible in the BBR and indicates the preferred pathways by which materials arrive inshore. A summary and some concluding remarks are presented in section 6.

2. Models and Forcing

a. Description of the ocean model

The Regional Ocean Modeling System (ROMS; Shchepetkin and Mcwilliams, 2003, 2005) is configured with a uniform 1/120° (800—900 m) grid spacing that extends north of 28°N and east of 86.75°W to the Florida coastline (see Fig. 1). ROMS is a free-surface, terrain-following, primitive equation ocean model that is frequently used for shelf and coastal applications (Shchepetkin and Mcwilliams, 2005). The terrain-following vertical s-coordinate of ROMS provides a constant number of layers that effectively increases the vertical resolution of the model over shallower depths. Although the nonalignment of the vertical coordinate isosurfaces to isopycnals or geopotential surfaces may lead to erroneous mixing in association with the calculation of the horizontal pressure gradient (Marchesiello *et al*. 2009; Lemarié *et al*. 2011), advanced advection schemes and the choice of domain can limit these errors.

The BBR configuration of ROMS (henceforth BBROMS) uses a third order, upstream-biased advection scheme for momentum with a specifically designed predictor-corrector time step algorithm. This allows the generation of physically realistic steep gradients (Shchepetkin and Mcwilliams, 1998). Advection of tracers is computed using the multidimensional positive definite advection transport algorithm (MPDATA), which reduces numerical overshoots and spurious diapycnal mixing by use of a flux-corrector scheme (Smolarkiewicz, 1984). A splines density Jacobian is used for calculation of the horizontal pressure gradient (Shchepetkin and Mcwilliams, 2003), and the Mellor Yamada 2.5 turbulence closure scheme is used with improvements from the Kantha and Clayson stability function (Mellor and Yamada, 1974, 1982; Kantha and Clayson, 1994). The BBROMS topography uses the National Geodetic Data Center's 30 arcsec coastal relief dataset, to which a uniform Gaussian filter with a radius of 3 grid points is applied. Smoothing of steep gradients in the topography is done to satisfy suggested grid stiffness ratios related to the calculation of horizontal pressure gradient (Haney 1991; Beckman and Haidvogel 1993; and Sikiric *et al*., 2009). The smoothing of the topography and the choice of numerical schemes reduce potential errors caused by the calculation of the horizontal pressure gradient.

The model's initial conditions and temporally evolving open boundary conditions are provided by the 1/25° Gulf of Mexico HYbrid Coordinate Ocean Model (GOM HYCOM; Bleck, 2002; Chassignet *et al*., 2007, 2009, 2011). HYCOM uses the Navy Coupled Ocean Data Assimilation system (Cummings, 2005), which assimilates available satellite altimeter observations, satellite and in situ SSTs, and in situ vertical temperature and salinity profiles from XBTs, Argo floats, and moored buoys. The HYCOM's state-of-the-art prediction system provides a robust estimate of the ocean state that is well resolved in space and time, and may be applied as boundary conditions to the higher-resolution BBROMS (Barth *et al*., 2007, 2008; Chassignet *et al*., 2009).

The initial conditions at 01 January 2004 and the boundary conditions are prescribed using the temperature, salinity, sea surface height, and velocity fields from the GOM HYCOM (available as daily snapshots at 00 UTC) and are interpolated to the BBROMS grid using splines in the vertical and horizontal. The interpolated GOM HYCOM fields are then applied at the open boundaries using radiation conditions and with a nudging term that is imposed at the boundary and over a transition zone near the boundary. The model field over the transition zone is then adjusted to be a weighted combination of the initially computed BBROMS field and the field set by the GOM HYCOM. For example, the equation of the predicted fields has a term such as:

$$\frac{\partial A}{\partial t} = ... + T_{nudge}(A - A_0),$$

where A is the predicted value of temperature, salinity, sea level, or velocity from BBROMS, A_O is the corresponding field from the GOM HYCOM, and T_{nudge} is a relaxation time scale that follows the formula

$$T_{nudge} = \frac{1}{\tau} \exp(-x/15) \quad ,$$

where τ= 0.1 days and x is the number of grid cells away from the boundary. T_{nudge} ranges from a relaxation time scale of 0.1 days at the boundary to 10 days at 44 grid cells (~35 km) inshore of the boundary. Beyond 46 grid cells from the boundary, $T_{nudge} = 0$. The internal radius of deformation is a length scale over which significant features propagating into the region through the open boundary should be preserved and is roughly 35 km or ~44 grid cells. Flather boundary conditions are applied to the two-dimensional momentum variables normal to the boundaries, and Chapman boundary conditions are applied to the free surface to allow for gravity wave radiation (Flather, 1976; Chapman, 1985).

Nineteen rivers provide fluxes of momentum and low salinity water at the coast. River streamflows are prescribed using daily means from United States Geological Survey (USGS) gauges, and are applied as sources of constant low salinity (3 PSU). River temperatures vary as monthly climatology values, and streamflows are applied as linear profiles in the vertical, which allows a higher percentage of outflow at the surface.

The ocean model uses 10 m winds, air temperature, specific humidity, pressure, rainfall, and shortwave and longwave radiation to calculate momentum, heat, and freshwater fluxes from bulk formulae adapted from the Coupled Ocean-Atmosphere Response Experiment (COARE; see Fairall *et al.,* 2003).

Ocean model hindcast simulations are initialized from the GOM HYCOM on 01 Jan 2004 and run continuously for the period 2004—2010. Adjustment from the interpolated HYCOM fields used for initialization to the high resolution grid/topography and surface forcing occurs rapidly, within about two weeks from model start.

In addition to the hydrodynamic model, the Larval Transport Lagrangian Model (LTRANS; see North *et al*., 2008 and Schlag *et al*., 2008) is used to identify primary pathways for onshore transport of passive Lagrangian particles. With LTRANS, 156 passive Lagrangian particles are seeded every 3 hours for 12 weeks (104,832 particles per year) from pre-determined release locations between the 50 and 100m isobaths (see Fig. 1). Particle seeding begins at 00 UTC of 01 Feb each year, and particles are advected by the BBROMS depth-averaged velocity field. As will be discussed in section 4c, the depth-averaged fields are sufficient for use in this application. Each particle is followed for a maximum of 45 days, which corresponds to the mean gag pelagic larval duration. Particle trajectories are no longer followed once they reach the model boundaries.

b. Description of the atmospheric forcing datasets

Four different atmospheric models are used to force contemporaneous simulations using the BBROMS. All four atmospheric products are state-of-the-art prediction or reanalysis products that are constrained to observations through advanced data assimilation schemes. In addition to varying model physics and assimilation methods, each product provides a different combination of horizontal grid spacing and temporal resolution (see Table 1).

The Climate Forecast System Reanalysis (CFSR) and the North American Regional Reanalysis (NARR) are two datasets from the National Center from Environmental Prediction (NCEP). The CFSR, a global coupled ocean-atmosphere-land-sea ice modeling system that uses the NCEP Global Data Assimilation System, is described in great detail in Saha *et al*. (2006). It is the newest product of the four chosen atmospheric products, which is noteworthy in that it incorporates more data into its assimilation system (notably satellite scatterometer winds and direct assimilation of satellite-derived radiances). This product also provides the highest temporal resolution (hourly) of the four atmospheric datasets. The CFSR's hourly output fields are provided in the form of analysis fields every six hours, with hourly forecast fields for the intermediate time steps. The NARR is an atmospheric and land surface hydrology coupled model, which is run for regional application to North America at roughly 1/3° horizontal grid spacing and with analysis fields available at a frequency of 3 hours. The two main modeling components of NARR are the NCEP Eta atmospheric model and its associated 3D variational assimilation scheme, and the Noah land-surface model (for more details see Mesinger *et al*., 2006).

The Navy Operational Global Atmospheric Prediction System (NOGAPS) and the Coupled Ocean/Atmosphere Mesoscale Prediction System (COAMPS) are operational, data-assimilative models available from the Naval Research Laboratory (NRL; see Hogan and Rosmond, 1991; Rosmond, 1992; Hodur, 1996 for more details). The NRL's Central America COAMPS configuration is used, which is an uncoupled atmospheric model simulation that uses the Navy's multivariate optimally interpolated (MVOI) data assimilation system (Goerss and Phoebus, 1992; Barker, 1992) and provides the highest horizontal grid spacing of the four products at 0.2°. The NOGAPS also uses the MVOI data assimilation system and has the coarsest grid spacing of the four atmospheric products at 0.5°. Analysis fields for NOGAPS are provided every three hours. Since the NOGAPS is also used to force the GOM HYCOM, the inclusion of a NOGAPS-forced ocean model provides a simulation with consistent atmospheric forcing prescribed across the open boundaries.

Model runs forced with CFSR, NARR, and NOGAPS use the downward longwave radiation provided by each dataset and calculate the upward longwave radiative flux using the BBROMS surface temperatures assuming a surface emissivity of 97%. Since downward-only variables are not available for the Central America configuration of COAMPS, the COAMPS-forced BBROMS does not calculate the upward longwave radiative flux and instead uses net longwave radiative fluxes (downward minus upward). A +20 Wm^{-2} bias correction is added to the COAMPS net longwave radiative fluxes in order to correct for a cold bias caused by cooling associated with the prescribed surface radiation. All runs use the net shortwave radiation provided from their respective atmospheric forcing product.

c. Atmospheric forcing evaluation and variability

The winds from each atmospheric product are compared to data from three marine observation platforms in the NEGOM (National Data Buoy Center buoys 42036 and 42039 and tower SGOF1; see Fig. 1) over the period 2004—2010 to assess their accuracy in estimating the wind over the BBR. This comparison is intended to evaluate each model's performance over the study region rather than an independent validation of the models, as these data are assimilated into each product. Observed winds are adjusted to 10m above the surface using height adjustment procedures outlined by Liu and Tang (1996). All winds are low-pass filtered using a cosine-Lanczos filter (similar to Maksimova and Clarke, 2013), which passes 10% power at frequency 2π/30 hours (resulting in sub-inertial or low frequency variability).

A list of the correlation coefficients and parameter estimates from a least-squares fit of modeled wind speeds to observed wind speeds over the entire 7-year period of 2004—2010 is given in Table 2. Regression slopes that are close to unity indicate that CFSR, COAMPS, and NOGAPS all estimate the strength of the observed winds well at sites 42039 and SGOF1. At these sites, COAMPS and NOGAPS wind speeds in the high wind environment are underestimated by less than 1 ms^{-1} and are overestimated by only 0.4–0.6 ms^{-1} in the low wind environment. COAMPS captures the variability at all observation locations well, with all R^2 values above 0.82. CFSR winds at SGOF1 and 42036 are highly correlated ($R^2 \geq 0.93$) and a regression slope that falls very close to unity (>0.95, indicating that CFSR estimates the strength of the winds well in the mid to high wind strength environment). However, stronger winds near 42036 are underestimated by CFSR by about 1 ms^{-1}. Despite the underestimation of winds at 42036, CFSR accurately captures the variability of the winds at this location ($R^2 > 0.9$). Small regression slopes with intercepts near zero indicate that NARR has a systematic weak bias across the NEGOM, particularly in the high wind environment. Despite this weak bias, NARR captures the variability in the observed winds at every location well, with R^2 values between 0.81 and 0.84.

Winds during spring months originate most frequently from the east (28.6—30.4% of the springtime from the NE quadrant and 31.4—33.4% from the SE quadrant), as demonstrated by longer bars from the east in wind stress roses (Fig. 2). Winds from the northwest quadrant are less frequent (21—24% of the time), although the lengths of the bars in the strong wind environment during this wind regime demonstrate that these winds are considerably stronger than winds from any other direction. Winds from the southwest quadrant are both less frequent (occurring only 15.0—15.7% of the time) and weaker. These patterns hold particularly true for the wind stress provided by runs forced with COAMPS, NARR, and NOGAPS. However, the stronger wind stresses (> 0.2 $\mathrm{Nms^{-1}}$) from the run forced with CFSR are observed across a wider range of directions. The wind stresses from the NARR-forced run are weaker everywhere, and only a small percentage of the wind stresses are greater than 0.2 $\mathrm{Nms^{-1}}$. The patterns exhibited in Fig. 2 are consistent with the idea that the dominant frequency of variability in the springtime wind stress occurs in the synoptic band. Pre-frontal winds originate from the southeast and, upon the passage of the cold front, quickly rotate to the northwesterly quadrant, where they are typically stronger. Then, the winds slowly rotate back toward the east.

The strength and the frequency of the alongshore component of the wind stress correlate well with the dominant shelf flow features (Mitchum and Clarke, 1984; Maksimova and Clarke, 2013). To compare the strengths and frequencies of springtime winds acting over the BBR from each atmospheric product, the modeled wind stresses are extracted from a point near buoy 42036 and rotated to 30 degrees west of north, an angle that roughly follows the orientation of the continental shelf break across the WFS and the semimajor axis of the wind stress' standard deviation ellipses (see Fig. 4 from Maksimova and Clarke, 2013). The wind stresses are low-pass filtered using a 2-day running mean, and power spectra density within the synoptic band

(3—10 days) for each model run are calculated for February—May of each year (Fig. 3). A consistent peak in power spectra is observed around 3—4 days each year, with the mean and standard deviations in the period of local maxima in the power spectra 4.4 days and 0.7 days, respectively. In all years, the power significantly drops off at frequencies less than 1 cycle per 3 days, demonstrating that dominant mode of wind stress variability occurs at synoptic time scales around 4 days. A second and larger peak around 5 days occurs in 2004 and 2005, and there is not a defined peak within the 3—5 day band for 2008 and 2009. However, high-pass filtering the data elucidates this particular peak in the power spectra during these years. The reduced power for NARR wind stress in Fig. 3 highlights the previously discussed weak bias in this atmospheric product's winds over the BBR.

3. Big Bend Circulation

The mean flow features of the BBR are described in the following section using the four contemporaneous ocean model simulations. First, the ocean model simulations are validated through a comparison of various model fields to regional observations. Then, the mean springtime flow features are described. Finally, the variability of the flow is discussed on various time scales, providing a description of the major components of the BBR circulation.

a. Model validation

The four contemporaneous ocean model simulations are compared to a suite of regional observations from coastal sea level gauges, surface buoys, satellites, and bottom-mounted current profilers. Three coastal sea level gauges are located within the model domain at Cedar Key, Apalachicola, and Panama City. Surface temperatures are available from buoys 42036 and 42039 and tower SGOF1. Satellite-derived temperatures are provided by the Multi-sensor Improved Sea Surface Temperature (MISST) product, which blends observations from the MODIS, TMI, and AMSR-E satellite radiometers (Gentemann, 2009). Finally, the model velocities are compared with two current profiler time series at site N7 and site S (Fig. 1). Observed and modeled sea levels and currents are filtered using the previously mentioned cosine-Lanczos filter. Lunar and solar fortnightly tides are removed from observed sea level and current measurements using a least squares fit before applying the filter.

i. Sea level

The simulated sea level anomalies are compared to data from three coastal tide gauge stations operated by the NOAA Center for Operational Oceanographic Products and Services. Observed sea level anomalies are referenced to their 1981—2001 mean, and simulated sea level anomalies are referenced to the simulation-long mean (01 Jan 2004—31 Dec 2010). Each BBROMS simulation reproduces variations seen in the coastal sea level anomalies data well, with correlations over all the spring months greater than 0.85 for Panama City and Apalachicola, and greater than 0.65 for Cedar Key. Time series of modeled and observed subinertial sea level anomalies are compared near Panama City in Fig. 4. The springtime root mean squared error (rmse) falls below 8.5 cm for all model simulations, with the exception of 2010, when each contemporaneous model simulation has a bias toward lower sea level anomalies with increased rmse of about 11 cm. This year was a warm El Niño/Southern Oscillation (ENSO) phase year (an El Niño year). Warm phase ENSO years experience increased atmospheric cyclogensis over the GOM compared to years with near-neutral or cold ENSO phases, due to the positioning of 300 hPa jets over the GOM and a shift of the Bermuda High well eastward of the continental

United States (Smith et al., 1998; Kennedy et al., 2007). This increases the occurrence of cyclones that progress eastward across the GOM and consequently increases the frequency of low sea level events over the Eastern GOM (Kennedy et al., 2007). The variability of modeled sea levels remain highly correlated with the observed sea level anomalies during 2010, with correlation values greater than 0.8, 0.7, and 0.74 for Panama City, Apalachicola, and Cedar Key, respectively.

ii. Temperature

Annual mean surface temperatures are obtained from each contemporaneous model run, the 9 km MISST, and from the GOM HYCOM. Since the MISST signal is contaminated by land near the coast, surface temperatures from each model simulation are only taken from points across the domain for which the MISST grid returns valid SSTs. All models produce annual mean surface temperatures that follow the mean trends observed from the 9 km MISST. The trend in the annually and spatially averaged model SSTs follow the same pattern as those observed from MISST, with CFSR- and NARR-forced models fitting well within the observational error bounds provided by MISST (Fig. 5). BBROMS simulations forced by NOGAPS and COAMPS show a bias toward colder annual mean SSTs when compared to the MISST, with mean temperatures dropping below the observational error of MISST in 2009 and 2010. HYCOM also demonstrates a cooler bias during these two years compared to the mean, although the annual means remain within the observational error. The cold bias observed with COAMPS and NOGAPS is due to colder mean SSTs during fall and winter months, as these two simulations closely match the MISST during the spring and summer. The mean SSTs from simulations forced by CFSR and NARR closely match MISST from fall through the spring, although they are overestimated during the summer. The greatest cooling (warming) in the winter (summer) occurs near the coast where satellite retrievals are poorer due to land contamination. Regardless, each model reproduces the annual mean SSTs within ±0.5°C.

The models more accurately reproduce surface temperatures at regional buoy observations, where comparisons of three-hourly surface temperature data indicate that R^2 values all exceed 0.93 and linear regression fits fall very close to the unity line (see Table 3), demonstrating that the models capture the high-frequency and submesoscale variability of the surface temperatures across the domain.

iii. Currents

Velocities from each contemporaneous model simulation are compared to observed velocities from two bottom-mounted current profilers at depths of 19 m southeast of Apalachicola Bay at site N7 and at site S (Fig. 1). These observations are the only available *in situ* velocity measurements in the region over the time period of interest, and Maksimova and Clarke (2013) describe their seasonal and interannual variability in detail. A bottom-mounted Acoustic Doppler Current Profiler (ADCP) was deployed at site N7 on Jan 2007 and a bottom-mounted acoustic wave and current (AWAC) profiler was deployed at site S from 23 April 2009 to 9 July 2010. The bottom-mounted ADCP has a blanking distance of 4 meters and measurements are averaged into 1-m vertical bins. Surface data contamination occurs in the uppermost three meters, and therefore velocities in this surface layer are removed and unavailable for analysis. The velocities observed using the AWAC are resolved in 1-m bins from 1 meter above the bottom (mab) to 16 mab, roughly 3 meters below the surface. The data record for site N7 covers 96% of the period from deployment to 8 October 2010, and only a very small gap exists between deployments at site S during November 2009 (resulting in 97% coverage).

Lunar and fortnightly tides are removed from the observed velocities at site N7 and site S using a least squares fit. All velocities are then filtered to subinertial frequencies and are rotated to alongshore and cross-shore components. The alongshore axis is defined as the semimajor axis of the standard deviation ellipse for depth-averaged flow, and is calculated independently for each dataset or model simulation. In similar fashion, the cross-shore currents are defined along the semiminor axis of the flow. Correlations between modeled springtime alongshore or cross-shore currents and the observed currents are generally near or exceed 0.7, indicating that the variability of the observed flow is captured well by the model simulations (Figs. 6 and 7). The exception is for the NARR-forced run, whose springtime correlation values fall below 0.5 in 2008 and below 0.6 for along-shore currents in 2010. The interquantile range (the difference between the 20^{th} and 80^{th} percentiles) of the flow at N7 demonstrates that the variability in the observed alongshore currents ranges from as low as 5 cm s^{-1} near the bottom to almost 20 cm s^{-1} near the surface, with an interquantile range of the depth-averaged flow at about 10 cm s^{-1} (Fig. 8). The interquantile range of cross-shore currents varies from 5 to 10 cm s^{-1} in 2007–2009, although the cross-shore flow is stronger (particularly near the bottom) in 2010, when the interquantile range increases to 12 cm s^{-1} at 6 mab. The average range of variability is much larger than the means at each depth, which are at least an order of magnitude smaller on average (Fig. 8), and the depth-averaged interquantile ranges for alongshore flow are 30 times larger than the means.

The overestimation of the stronger flows is reduced at site S, where the current speeds are weaker overall in 2010 (the interquantile range is 3—15 cm s^{-1}). At this location, the spread among the models' depth-averaged velocity time series is narrower and they collapse onto the observed velocity time series (Fig. 9). The correlations remain within the same range as those observed at site N7 in 2010; runs forced by COAMPS and CFSR exhibit high correlations ($R > 0.8$) and the NOGAPS-forced simulation exhibits lower correlations ($R \sim 0.66$). The NARR-forced simulation captures only 60% or less of the variability in observed currents.

b. Mean shelf circulation features

All four contemporaneous simulations reproduce several distinct mean flow features. A surface-to-mid-depth concentrated jet flows northwestward along the continental slope (Figs. 10—12). This slope jet is not present in the simplified WFS model presented by He and Weisberg (2002b), and it flows in the opposite direction to the jet proposed by Hetland *et al.* (1999) and observed further south by He and Weisberg (2003). The northwest-flowing current is however consistent with the flow provided by the open boundary conditions via the GOM HYCOM. Since He and Weisberg (2002b) neglect LC forcing during their study period of March—May, and Hetland *et al.* (1999) use a hypothetical LC setup, these studies are not able to capture the variability in LC position and extent. Furthermore, the work by He and Weisberg (2003) consider flow much farther south, which does not exclude the possibility of a northwestward-flowing slope current in the BBR. Therefore, the strong flow offshore of the shelf break is attributed to deep ocean fluxes set by the open boundary conditions (an idea that is consistent with that proposed by He and Weisberg, 2003).

Adjacent to this area of northwesterly flow along the slope, there is a distinct separation in flow patterns between the circulation on the shelf and the circulation over the continental slope and deep ocean. Between the two regions, the mean vertically averaged currents change direction by 180 degrees across a narrow region of about 15—20 km at the shelf break. This is consistent with the finding by He and Weisberg (2003) that the deep ocean influences the shelf circulation only within a radius of deformation of the shelf break. Therefore, since this study is concerned with the wind-driven flow on the shelf and not the flow seaward of the shelf break, which is set mostly by the deep ocean, the following discussion focuses only on those features shoreward of the shelf break.

Perhaps the most striking feature of the mean vertically averaged velocities is the area just offshore of Cape San Blas and Cape St. George. The mean flow in this area exhibits a banded structure of onshore currents juxtaposed with areas of offshore currents, where the mean cross-shore currents extend from the coastline to nearly the shelf break. These features are observed in the vertically averaged velocity fields and at all depths (Figs. 11 and 12).

Inshore and eastward of this region, close to the barrier islands that separate Apalachicola Bay from the GOM, the mean flow is cross-shore and vertically sheared, with opposing surface and bottom velocities directed offshore and onshore, respectively (Figs. 11 and 12). The near-surface velocity field highlights the influence of the BBR rivers on the near-coastal surface circulation, as surface velocities are generally directed outward from Apalachicola Bay. The less saline surface waters flow adjacent to the coastline and to the right (toward the west) in the absence of northerly or westerly winds (Lentz, 2012). These less saline waters are occasionally advected toward the south and east under northerly or westerly winds and can provide a conduit for less saline and nutrient-rich waters to reach the mid-shelf. The offshore flux of high nutrient water from the Apalachicola River has been linked with the observed high cholorphyll content surface waters several hundred kilometers south along the mid-WFS (Gilbes *el al*., 1996; Morey *et al*., 2009). Although the mean surface velocity field is directed outward from all the passes in

Apalachicola Bay, the direction of the flow at any given time varies considerably and the southward and eastward reach of the buoyant surface waters relies on a specific combination of winds from the north or west. The mean near-bottom velocities inshore of the 20 m isobath in this region are directed toward the coast, particularly at the eastern end of Apalachicola Bay, highlighting the vertical shear in the region directly influenced by the rivers.

Along the eastern portion of the BBR, the mean alongshore flow within the 20 m isobath is mostly barotropic and directed toward the southeast. He and Weisberg (2003) describe a southeastward-flowing shelf jet that bifurcates at Cape San Blas into a shelf-break jet and a coastal jet. Although an organized southeast-directed coastal flow is seen in the 7-year means of Feb—May circulation from each BBROMS simulation, a shelf-break component of this flow is not observed. Instead, the shelf break component mostly vanishes immediately south of the region where He and Weisberg (2002b) observe a bifurcation. The weakening of the jet modeled by the BBROMS is likely induced by the spreading of the isobaths southeast of the Cape San Blas, which, by conservation of momentum, would require the flow to weaken as it spreads out over the wider WFS. Velocities are very weak on average over nearly the entire midshelf in the widest portion of the BBR.

There are few differences between the mean flow fields of each contemporaneous BBROMS simulation. All of the dominant flow features described above are present in each simulation, and the widths, directions, structure, and locations of these features all closely match. The largest difference between the model runs arises with the NARR-forced BBROMS. Although the mean features of this simulation match the other simulations, it does not capture the variability of observed currents well (evident through the reduced correlations as compared to observed currents at site N7 and site S) due to the systematic weak bias in NARR wind stress.

Otherwise, the CFSR-, COAMPS-, and NOGAPS-forced BBROMS simulations all match closely and have correlations with observed currents that generally exceed 0.7. The minor differences between the mean flow features of each BROMS simulation indicates that the mean spring BBR shelf circulation responds primarily to the large-scale, subinertial wind stress, and does not vary considerably with smaller spatial or temporal scale variability in the wind stress. To limit the discussion of the variability of the flow on multiple time scales, the CFSR- forced BBROMS simulation is chosen as the representative model as it consistently provides the highest correlations when compared to the different observational data. Therefore, the analysis and discussion of flow features and transport in the BBR will use the output from only the CFSR-forced BBROMS.

e. Flow variability

Although the dominant mode of variability for the spring circulation occurs at synoptic time scales, there is some interannual variability of the major shelf circulation features (Fig. 13). The dominant flow features described above persist from year to year, although the relative magnitudes of those flow features may vary. In particular, stronger cross-shelf flow offshore Cape San Blas and Cape St. George is observed in 2005, 2007, and 2010. Although these cross-shelf flow features are stronger in these years, it is the onshore-flowing regions where the most distinct enhancement occurs; this is especially true for the onshore-flowing region south of Apalachicola Bay. The most pronounced flow enhancement occurs in 2010, when the mean shelf circulation features are stronger offshore of Cape San Blas and Cape St. George and throughout the coastal jet. The slope jet is not nearly as prevalent in 2005 and 2010, and the offshore extension of the onshore flow south of Cape San Blas could affect the slope jet in this region. The coastal jet vanishes in the spring mean for 2008 and 2009.

Section 2c demonstrates that the dominant frequency of wind stress variability occurs at synoptic scales during the spring season, mostly in association with the passage of atmospheric cold fronts. These frontal passages have prefrontal phases of southeasterly winds (downwelling-favorable) and postfrontal phases of northwesterly winds (upwelling-favorable). By dissecting the ocean circulation into flow during each of these two different wind regimes (i.e., averaging the spring velocities during winds from N-W or during winds from S-E), the two dominant flow patterns during the springtime circulation are captured (Fig. 14). Averaging the spring velocities during only northwesterly winds (top panel of Fig. 14) yields a strong southeast-directed shelf flow that is enhanced over the three regions offshore of Cape San Blas and Cape St. George where cross-shelf flow is observed in Figs. 10—12. Averaging the spring velocities during only southeasterly winds (bottom panel of Fig. 14) yields a weaker northwest-directed shelf flow and slope jet, with flow enhancement existing only over one small region offshore of Cape San Blas. Over the midshelf, velocities during each wind regime flow along-isobath and in directions that roughly oppose each other.

Averaging the flow during northwesterly winds and southeasterly winds (the average of the two dominant flow patterns) produces a depth-averaged flow field in which all of the features present in the full spring mean are retained (compare Fig. 15 to Fig. 10). That is, the cross-shelf flow offshore of Cape San Blas and Cape St. George, the southeastward-flowing coastal jet, and the northwestward-flowing slope jet are each present in the conditionally averaged flow. Thus, the cross-shelf velocities offshore Cape San Blas and Cape St. George and the coastal jet are simply the rectification of two asymmetric, yet opposite flows during oscillating upwelling-favorable and downwelling-favorable winds. The flow during northwesterly winds is enhanced over the region from Cape San Blas shoal to Cape St. George shoal, and the same flow enhancement is not observed during southeasterly winds. Therefore, the average of these two flow patterns is directed cross-shore in this region, and the observed interannual variability in the strength of the flow features is a direct result of the variability in the large-scale, low-frequency wind stress over the BBR. A similar flow rectification occurs in the coastal jet, although the flow here is directed mostly along-isobath during both wind regimes; it is simply the stronger flow during northwesterly winds that prevail when averaging the two flow patterns.

4. Cross-shelf transport mechanisms

a. Potential vorticity mechanisms

Flow that crosses isobaths must exhibit some change in its absolute vorticity; this may occur as a modification to its relative vorticity, as latitudinal movement, or as a stretching or a tilting of the fluid column. The degree of modification of each component of the vorticity may differ depending on the response of the ocean to the wind forcing. The dominant flow features described in section 3 are present at all depths of the water column, suggesting that the ocean responds barotropically to the large-scale, low-frequency wind stress. This was also found to be the case for the WFS (Clarke and Brink, 1985). The Burger number, an indicator of the baroclinicity of the flow's response, is used to verify that the flow should indeed respond barotropically, and is defined as

$$Bu = \frac{N^2 H^2}{f^2 L^2} = \left(\frac{R_D}{R_C} \right)^2 \quad , \tag{1}$$

where L is a length scale defined to be the radius of curvature of the topography, R_C, $R_D=NHf^{-1}$ is the Rossby radius of deformation, $N=\left[\left(-g/\rho_0\right)\partial\rho/\partial z\right]^{1/2}$ is the Brunt-Väisälä (buoyancy) frequency, ρ is the density, ρ_0 is a constant reference density, H is the undisturbed water depth, and z is the vertical coordinate. The Burger number therefore characterizes the interplay between the stratification, shelf geometry, latitude, and the characteristics of the forcing (Dukhovskoy *et al.*, 2009). Thus, if $Bu << 1$, the flow response can be considered to be barotropic, whereas $Bu >> 1$ implies strong baroclinicity to the ocean response. For springtime flow over the BBR, the mean Burger number over the shelf (shallower than 200 m) is $O(10^{-3}) << 1$, indicating that the response should be barotropic (consistent with Clarke and Brink, 1985).

Since the flow is expected to respond barotropically to the wind forcing, the shallow water equations may be used to describe the flow features in the region. That is,

$$\frac{\partial u}{\partial t}+u\frac{\partial u}{\partial x}+v\frac{\partial u}{\partial y}-fv=-\frac{1}{\rho}\frac{\partial p}{\partial x} \tag{2.1}$$

$$\frac{\partial v}{\partial t}+u\frac{\partial v}{\partial x}+v\frac{\partial v}{\partial y}+fu=-\frac{1}{\rho}\frac{\partial p}{\partial y} \tag{2.2}$$

$$\rho g=\frac{\partial p}{\partial z} \tag{2.3}$$

$$\frac{\partial u}{\partial x}+\frac{\partial v}{\partial y}+\frac{\partial w}{\partial z}=0\ , \tag{2.4}$$

where u, v, and w are velocities in the x, y, and z-directions, respectively; f is the Corliolis parameter; p is the pressure; and g is the local gravitational acceleration. From these equations of motion, a relationship for the potential vorticity (PV) of the flow under the influence of frictional vertical boundary layers may be derived. That is, if *f*-plane and rigid lid approximations are used, then equation 5.2.20 from Pedlosky (1987) may be re-written in dimensional form as

$$\frac{d}{dt}\left(\frac{\zeta+f}{h}\right)=\left(\frac{\zeta+f}{h^2}\right)\left[\frac{1}{\rho}\hat{k}\bullet\vec{\nabla}\times\left(\frac{\vec{\tau}}{f}\right)-\frac{\delta}{2}\bar{\zeta}\right], \tag{3}$$

where $h(x,y,t)$ is the distance from the free surface to the bottom $b(x,y)$, τ is the stress at the bottom of the surface boundary layer, δ is the boundary layer thickness, $\bar{\zeta}=\partial\bar{v}/\partial x-\partial\bar{u}/\partial y$ is the mean relative vorticity in the boundary layer (bars denote boundary layer averages), and $q=(\zeta+f)/h$ is the PV. So, if PV is conserved in time, then the right-hand side of equation (3) is zero, such that

$$\frac{d}{dt}\left(\frac{\zeta+f}{h}\right)=\frac{dq}{dt}=0\ . \tag{4}$$

However, it is clear from equation (3) that the frictional effects of the boundary layers inhibit the conservation of PV over time. Therefore, equation (3) may be used to estimate a time scale over which the effect of frictional boundary layers becomes important, or the time scale at which conservation of PV no longer occurs. The ocean's response to external forcing is considered by neglecting any additional input to the system ($\tau \rightarrow 0$), reducing equation (3) to

$$\frac{dq}{dt}=\frac{\delta\bar{\zeta}}{2h}q\ . \tag{5}$$

Equation (5) indicates that the frictional effects of the boundary layer cause a damping of the flow that scales as $(\delta/2h)\bar{\zeta}$. The vorticity of the flow at the top of the bottom boundary layer must equal the vorticity of the interior flow, and must be zero at $z=h+b$; therefore, $\bar{\zeta}\approx\zeta/2$, where ζ is the mean value of vorticity over the interior of the water column. So, the damping of the flow occurs over the time scale given by

$$T \sim \frac{4h}{\delta\zeta} \geq \frac{4h}{\delta f} \quad \text{if} \;\; \zeta \leq f. \tag{6}$$

A few characteristics of the shelf flow may be inferred from this damping time scale. First, the frictional damping increases in shallow water (decreasing h indicates a decreasing time scale). Also, the damping time scale is generally greater than ¼ pendulum day (~12 hrs at 30° latitude) if $\zeta < f$. However, the formulation of the PV given by equation (3) becomes invalid when the surface and bottom Ekman layers begin to interact. The overlapping of Ekman layers occurs roughly where h=3δ (Mitchum and Clarke, 1986). A log layer assumption for the boundary layer yields an estimate of $\delta \sim 5—10$ m. Therefore, the approximation for the damping time scale is valid until the nearshore region where $h \sim 15—30$ m. Equation (5) also indicates that the frictional damping enhances the extraction of PV from the flow in shallower areas. When the flow is farther offshore, the frictional damping takes longer to extract PV from the system (increasing h means larger T), and therefore the flow is more able to conserve PV. Finally, for time scales less than 12 hours over much of the shelf, the flow tends to conserve PV. Over longer time scales and in shallower waters, extraction of PV from the system via the frictional boundary layers causes the right-hand side of equation (5) to be significant, thereby inhibiting conservation of PV. The following sections will demonstrate that the nonconservation of PV enhances the onshore transport in areas with cross-isobath flow and contributes to successfully moving particles across the shelf to the coast.

b. Eulerian analysis

The flow is expected to conserve PV via equation (4) over short time scales. This conservation of PV may occur if flow moves along contours of f/h. However, if the flow encounters an abrupt change in h, some relative vorticity must be introduced to the system for conservation to occur. Therefore, according to equation (4), the relationship between ζ and f determines whether the flow will conserve its PV when it encounters a change in depth. The relative vorticity may be scaled as $\zeta \sim V/R_C$ when the horizontal shear is weak (this is generally true for the two dominant flow regimes in the BBR; see Fig. 14). The relative vorticity plays an increasingly large role in governing the flow as $|\zeta|/f \rightarrow 1$, which occurs when the flow is strong ($|V|$ large) or when the flow tightly curves (R_C is small over tightly curving isobaths). For flow that is weaker ($|V|$ small) or for gently curving flow (R_C large), $|\zeta|/f \rightarrow 0$ and so Coriolis dominates. For this case, the flow should follow contours of f/h. At any given location on the shelf, f and $|R_C|$ do not change, and so the greater magnitude of ζ/f for northwesterly winds in Fig. 16 indicates that the stronger flow during these winds is more likely to cross isobaths and therefore induce relative vorticity to the flow.

To better depict the process by which currents may conserve PV in the BBR, consider the southeastward-flowing currents during northwesterly winds. As this strong flow moves from the NW panhandle, it encounters the shallow waters of the Cape San Blas shoal (where h quickly decreases) and must add negative ζ by turning to the right (in the offshore direction). The rapidly curving isobaths in this area cause the offshore-flowing current to quickly encounter deeper water (increasing h), which then requires the flow to induce a positive ζ and consequently turn to the left (onshore). The shelf geometry offshore Cape San Blas and Cape St. George causes this process to repeat once more before the flow adjusts to the wider, gently curving shelf east of N7 and moves along-isobath. The areas where contours of f/h and PV intersect and separate during this flow regime in Fig. 14 therefore indicate the locations where PV-conserving flow is expected to cross isobaths. The crossing of isobaths occurs in conjunction with the change in sign of ζ/f, which can only change sign with ζ. Fig. 16 depicts this example of PV-conserving flow during northwesterly winds.

Flow during southeasterly winds is weaker, thereby providing smaller magnitudes of ζ/f. This weaker northwestward flow is then able to quickly adjust to the tightly curving isobaths, reducing the need to add significant relative vorticity to the flow to conserve its PV. For this reason, the contours of f/h closely match contours of PV during this flow regime, with the exception of the region of very tight curvature over the Cape San Blas shoal. Thus, flow during this wind regime can also be expected to conserve its PV because weaker flow reduces the potential for cross-shore movement.

c. Lagrangian analysis

Incongruity between contours of PV and f/h suggests that the flow conserves its PV by adjusting its relative vorticity when crossing isobaths. The validity of this assumption is assessed using a Lagrangian analysis. Equation (4) may be evaluated at two consecutive time steps *t* and $t+\Delta t$, such that

$$\left(\frac{\zeta+f}{h}\right)\bigg|_{t}=\left(\frac{\zeta+f}{h}\right)\bigg|_{t+\Delta t} \tag{7}$$

or

$$\frac{\zeta+f}{h}=\frac{(\zeta+\Delta\zeta)+f}{h+\Delta h}, \tag{8}$$

which, assuming changes in f from one time step to another are negligible (f-plane approximation is valid for this application), reiterates that flow moving over sharply changing bathymetry must induce some relative vorticity to conserve its PV. Rearranging equation (8) reveals the relationship

$$\frac{\Delta h}{h} = \frac{\Delta \zeta}{\zeta + f} \ , \tag{9}$$

which indicates that the fractional change in depth of the flow from one time step to another should be balanced by a corresponding change in relative vorticity if PV is indeed conserved. The strength of this relationship is tested by tracking the evolution of the depth and relative vorticity in the flow through time, thereby analyzing whether the flow conserves PV. This is accomplished using the Lagrangian particle advection model, whose implementation is described in Section 2a.

The time evolution of a parcel of water flowing in a PV-conserving system should follow the relationship given by equation (9). Since the flow is mostly barotropic, the Lagrangian particles' vertical positions are neglected and they are advected in the depth-averaged flow field. Thus, each particle is considered to be a parcel of water covering the depth of the fluid column. The time-evolution of each side of equation (9) is calculated for each particle at three-hour intervals. The estimates of the frictional damping given by equation (5) suggest the flow should be expected to conserve PV on this short time scale. Upon calculating both sides of equation (9) particle trajectories, the averages of each side are calculated for all particles within 0.05° × 0.05° bins across the BBR modeling domain. When contoured together (Fig. 17), areas of high and low values of each side of equation (9) are co-located and are of comparable sign and magnitude. This clearly shows that cross-shore movement of the flow is generally balanced by the addition of relative vorticity of the same sign and magnitude. Both the signs and the magnitudes of each side of equation (9) match well across all the areas in which significant cross-shore flow is observed (Fig. 10). The exception to this agreement in Fig. 17 occurs in areas where there is commonly freshwater outflow from the Apalachicola River (i.e., to the west of Cape San Blas and at the west end of Apalachicola Bay). Buoyant water originating from the river frequently exists in this area, enhancing the stratification and therefore invalidating the barotropic assumption used in equation (4). Regardless, both sides of equation (9) agree in the areas where considerable cross-shore flow occurs, the main areas of interest for this study. Therefore, the barotropic flow on the BBR shelf generally conserves its potential vorticity on short time scales, which allows for cross-shore movement during flow associated with strong northwesterly wind events.

Potential vorticity is less likely to be conserved over longer time scales. If PV is not conserved, then particles will not be required to follow PV contours, and are then able to be distributed across the entire domain. The spatial distribution of particles during their advection period and the variability in their distribution are examined. Since over 730,000 particles are tracked over the 7-year experiment, one cannot determine the preferred locations of advection by comparing individual particle trajectories. Therefore, the domain is divided into $0.1° \times 0.1°$ boxes, and the percentage of particles to pass through each box during their advection period is calculated (henceforth referred to as "particle track density").

The particle track densities provide a metric by which one can identify the preferred particle advection pathways. Fig. 18a shows the density of particle trajectories over the entire seven-year advection period (that is, the fraction of all particles that ever pass within each bin). The highest percentage of particles appears along the shelf break, where the particles are seeded and transported northwestward in the slope jet. It is evident that the slope jet provides the primary flow of particles, as the percentages are skewed toward higher values along the shelf break in the northwest portion of the domain compared to values along the shelf break near the southern boundary. Because of this northwestward flow, 39% of all particles leave the domain through the western boundary, while 17% leave through the southern boundary. Therefore, even though half of the particles remain inside the domain during their advection, the primary location for particles to exit the domain is through the western boundary via the slope jet. However, particles are able to cross isobaths and move onshore (or offshore) during upwelling-favorable winds via the balance of PV, reiterating that southeasterly winds (and hence northwestward flow) are more frequent during the spring, but the northwesterly winds (and their ability to drive cross-isobath flow) can contribute significantly to the overall distribution of materials away from the shelf break. Fig. 18a also demonstrates that very few (~1%) particles arrive inshore of the 10-m isobath during their advection. Although an area of slightly higher particle track densities exists to the southeast of Cape St. George, the percentages in this area are less than 5%.

The distribution of the particles that are advected away from the shelf break undergoes considerable interannual variability (Fig. 18b-h). In particular, the tongue of higher particle density southeast of Apalachicola Bay varies in magnitude and extent each year, with the highest percentages of particles in this region in 2005 and 2010. During the stormy El Niño year of 2010, a high number of particles reach the nearshore region of the BBR; this is the only year when particles are spread over nearly the entire BBR, particularly along the midshelf to the southwest of Cedar Key. This region to the south of Cedar Key is generally void of particles during years 2004–2009, reinforcing its name as the ”Forbidden Zone” (Yang *et al*. 1999). In all other years, the onshore tongue of higher particle densities to the southeast of Apalachicola Bay is significantly diminished from the levels seen in 2005 and 2010. During 2004 and 2006–2009, the percentage of particles that are advected inshore along the barrier islands of Apalachicola Bay is less than 5%. In 2007, a widely spread tongue of higher particle density is observed to the south of Cape St. George with percentages that are 3–5% higher than observed in non-warm ENSO phase years (2004 and 2006—2009), although the tongue is laterally spread toward the east, limiting its onshore extent. Years with enhanced areas of particle track density to the southeast of Apalachicola Bay are consistent with the years when the cross-shore flow features are enhanced in Fig. 10. In particular, the width and the strength of the onshore-flowing currents in the mean velocity field are larger in years when higher numbers of particles travel through these areas. Regardless of the percentage of particles that pass through this region to the southeast of Cape St. George, it is clearly an area where particles prefer to travel when being advected away from the shelf break.

d. Pathways for onshore transport

The primary pathways for onshore transport may be deciphered by examining the spatial density of only particles that successfully reach the nearshore region at some point during their advection. The 10-m isobath is chosen as the nearshore region, as it provides a rough estimate of where seagrasses may occur in the BBR, which are the nursery habitat for juvenile gag grouper. The seagrasses exist in depths up to 20m, and at distances up to 50 km offshore (Iverson and Bittaker, 1986; Thompson and Phillips, 1987); however, their coverage is not always consistent or continuous, and they can be significantly affected by flood-stage river outflow and tropical storms (Carlson *et al.*, 2010). So, although seagrasses may not be continuous from the coast to depths of 10 m, other processes such as tides and buoyant river plumes may play more prominent roles in governing local flow features inshore of this depth. In addition, on the basis of the findings by Mitchum and Clarke (1986), equation (3) breaks down because of the overlapping of boundary layers at this depth. Finally, it was also suggested by Keener *et al*. (1988) that the flow features that govern both the advection and the behavior of gag larvae in the nearshore region might differ from the flow features that govern their advection offshore and over the shelf. Thus, the 10-m isobath is considered the nearshore region for the BBR.

Particle track densities are calculated for only those particles that arrive within the 10-m isobath at some point during their advection (henceforth referred to as ”successful” particles), and displayed in Fig. 19. Most successful particles pass through the area immediately to the south of Cape San Blas and Cape St. George where percentages are 50–80%. This is the same area with higher tongues of particle track density in 2005 and 2010 (see Figs. 18c and 18h), and is an area that exhibits significant onshore flow in the mean circulation (see Fig. 9). Very few successful particles travel to the south of about 28.8°N, demonstrating that the primary pathway by which particles are able to reach inshore is via the region immediately south of Cape St. George, where there are two areas of onshore-directed mean velocities.

The ability for the flow’s PV to be modified more effectively in shallower water has been demonstrated. Consider particles flowing in the springtime circulation, which oscillates between phases of northwesterly and southeasterly flow (see Fig. 20 for the trajectory of a particle released at 15:00 UTC on 11 February 2005). Flow toward the southeast is stronger and crosses isobaths near Cape San Blas and Cape St. George (28—35 Feb in Fig. 20). Particles that move onshore during this flow regime are carried in a flow that has PV extracted from it via the frictional boundary layers, modifying q. This causes the flow to ”forget” its original depth, particularly in shallow waters. However, when the flow regime shifts to northwestward flow, it conserves its PV by moving along isobath. This oscillation in flow patterns creates a ratcheting mechanism in which particles are able to move onshore during one flow regime, where the extraction of PV in the shallower waters allows particles to stay farther inshore. This ratcheting is clearly visible during the first 15-20 days of advection of the particle displayed in Fig. 20. The asymmetry in the two dominant flow patterns allows the flow onshore in one direction, but limits the cross-isobath flow in the other direction. Therefore, the presence of high successful particle track densities in the region with significant cross-shore flow suggests that particles move back and forth in this area in conjunction with the oscillatory flow patterns.

Since very few successful particles travel south of 28.8°N during their advection, are particles that originate along the southern parts of the BBR shelf break capable of reaching the nearshore environment? That is, do significantly more successful particles originate from a particular area? Understanding these questions will facilitate the identification of potential preferred spawning locations for particles, and indeed for gag larvae. There are 156 seeding locations chosen for this experiment along the shelf break in the BBR (Fig. 20). The trajectories of particles are traced to estimate the percentage of particles originating from each location that successfully reach the 10-m isobath. This analysis reveals that the seeding locations that produce the highest percentage of successful particles are south of Cape San Blas, in the region of tightly curving isobaths where significant cross-shore velocities are visible in the mean and adjacent to the region of highest successful particle density (Fig. 19). Over 15% of all the particles released in this area arrive inshore of the 10-m isobath at some point during their 45-day life. So, while only 1% of particles released from all locations arrive inshore, the highest percentage of successful particles predominantly originate from this area offshore of Cape San Blas. In fact, particles released to the south of 28.8°N or to the west of 86.1°W are largely unsuccessful at reaching the nearshore region (no particles released south of 28.5°N ever arrive inshore).

e. Application to gag grouper

The plight of pelagic larvae is that they only survive if they are fortunate enough avoid the harsh marine environmental factors such as potential predation, the lack of available food or suitable settlement substrate, or intolerable temperatures or salinities (Norcross and Shaw, 1984). This is evident because of the relatively small estimates of post larval ingress observed in relation to the fecundity of adult gag (Keener *et al*., 1988), but also because 99% of the particles released within the BBROMS domain never reach waters shallower than 10 m (where the vast majority of nursery habitat is found). So, while the percentage of particles that arrive within the 10-m isobath is low, it simply highlights the reliance of drifting particles on specific circulation features to provide their necessary transport inshore. Furthermore, the ability for these particles to arrive inshore can depend greatly on where they originate, as specific origins have significantly higher success rates (Fig. 19). The region with the highest successful particle rates also coincides with a known gag spawning aggregation site (the Madison Swanson Marine Reserve; Koenig *et al*., 2000). The co-location of the preferred release locations with a known gag spawning aggregation suggests that this area could be selectively chosen by gag as a spawning site because of its geographic proximity to areas where materials are more frequently transported into the suitable seagrass nursery habitats of the BBR.

Annual fecundity estimates for individual adult gag in the BBR range from about 65,000 to 61.4 million and vary by size and by age of the fish (Collins *et al*., 1998). An annual range of successful recruits may be estimated by assuming that the adult gag fecundity and the physical dispersal of eggs and larvae to suitable nursery habitats are the only variables that affect recruitment. Although these variables do not encompass the wide range of variables that may affect fish recruitment (i.e., food availability, predation, environmental stressors, three-dimensional circulation features, etc.), their use may provide an upper bound for recruitment estimates using depth-averaged physical transport. Therefore, if fish with this range of fecundity spawn anywhere in the BBR, the percentages of successful particles indicate that the physical circulation can successfully transport 1% inshore; this corresponds to 650–614,000 successful recruits per spawning adult. However, if fish with this range of fecundity spawn only in the region with high particle densities, then the physical circulation can successfully transport 15% inshore, corresponding to 9,750–9,210,00 successful recruits per spawning adult. These ranges reinforce the large range in variability in juvenile gag recruitment and demonstrate that other variables are also important in determining the variations in gag recruitment from year to year. However, even if 99.9% of eggs released were killed through various processes, the population of gag originating near Madison Swanson Marine Reserve would still see at least 10 recruits per individual spawning female given these simple estimates.

5. Summary and discussion

The BBR shelf waters responds to large-scale, low-frequency winds and smaller temporal or spatial scale variations in the winds do not have as significant of an impact on the mean circulation features. This is evident from the limited differences between the seven-year mean circulations from each contemporaneous simulation, despite the differences in spatial and temporal resolutions between each atmospheric forcing product. The main flow features observed in the seven-year mean springtime BBR circulation include a northwestward-flowing slope jet, a southeastward-flowing coastal jet, and several areas of cross-shelf velocities offshore of Cape San Blas and Cape St. George. The slope jet flow toward the northwest is set primarily by the deep ocean, but the flow on the shelf is set by the large-scale, low-frequency wind stress and generally responds barotropically to these winds. The mean cross-shelf velocities form a banded structure of offshore-directed flow adjacent to onshore-directed flow.

The hydrodynamic fields from the ocean model simulations are compared to several types of observations across the region. The model simulations all reproduce variations in sea level and surface temperatures that closely match the variability from observations at tide gauges ($R > 0.8$) or regional buoys ($R > 0.96$), respectively. When modeled velocities are compared to observed velocities at two different current meters located in depths of 19 m, the models capture the variability of subinertial velocities at both sites well ($R > 0.7$). The exception is the NARR-forced run, which poorly captures the variability demonstrated by the observed currents despite reproducing features in the mean circulation. This is a result of the systematic weak bias in the NARR winds.

The mean shelf circulation in the BBR is composed almost entirely of flow during two opposing wind regimes: winds from the northwest and winds from the southeast. Winds from easterly quadrants are much more frequent during the spring months, but northwesterly winds are stronger. These stronger, yet less frequent, northwesterly winds drive a correspondingly strong southeastward flow that is able to cross isobaths over regions where the isobaths exhibit tight curvature. Contrastingly, the flow during southeasterly winds is more frequent, but generally weaker. This weaker flow is able to more closely follow isobaths as it moves toward the northwest. The rectification of these two asymmetric yet opposite oscillating flows provides a mean flow that is directed cross-shore in the regions of tightly curving isobaths and is weak elsewhere.

Conservation of potential vorticity governs the flow over the BBR shelf on time scales shorter than roughly 12 hours. Advecting Lagrangian particles in the circulation demonstrates that the flow responds to changing ocean depths by inducing a compensatory change in relative vorticity. This indicates that, following PV conservation, the flow is able to cross isobaths during northwesterly winds. The strong flow during this wind regime quickly encounters shallower (deeper) depths and is forced to turn to the right (left) in the offshore (onshore) direction to add a compensating negative (positive) relative vorticity. However, flow from the southwest is weaker and quickly adjusts to changing isobaths without the need to induce a significant amount of relative vorticity. Over longer time scales (greater than ~12 hrs), PV may be extracted from the system through the frictional boundary layers, leading to nonconservation of PV. The frictional damping is enhanced in shallower waters, thereby enhancing the transport onshore. Therefore, nonconservation of PV provides a ratcheting mechanism that enhances the ability of particles to move into shallower water and comparatively restricts their offshore movement.

The Lagrangian particle trajectories also reveal the primary pathways that particles follow during their advection in the springtime circulation. Higher particle densities along the shelf break reveal that the primary pathway for advection is along the northwest-flowing slope jet, with advection away from the shelf break occurring because of the cross-isobath flow during northwesterly winds. There is considerable interannual variability in particle density patterns, particularly the distance onshore that particles are able to reach. However, the cross-isobath movement is limited, and only a small percentage of particles are able to make significant progress inshore. The years when higher percentages of particles are advected away from the shelf break correspond to years when the strength and width of mean cross-shore current features are increased.

Fifty to eighty percent of successful particles travel south of Apalachicola Bay at some point during their advection. This indicates that successful particles are carried inshore through this primary pathway to the south of Cape San Blas and Cape St. George and farther alongshore via the coastal jet. More particles follow this onshore tongue in the two positive ENSO phase years within this study (2005 and 2010), indicating that the strength and sign of ENSO phase could have an impact on the magnitude of cross-shore transport in the BBR. However, a larger time record is needed to make any definitive conclusions of the impact of interannual or interdecadal oscillations on transport patterns in the BBR.

Finally, a preferred origin for successful particles exists to the southwest of Cape San Blas. This preferred origin for successful particles is immediately adjacent to the region of high successful particle density, to the locations with mean cross-shore currents, and to a known gag spawning site, the Madison Swanson Marine Reserve. The location of this preferred origin for successful particles leads to some interesting biological questions, including whether or not gag have chosen this location as a preferred spawning site because of the increased ability of materials originating from this area to arrive inshore.

The findings presented in section 4 reiterate the importance of the Madison Swanson Marine Reserve as a spawning aggregation site. The Madison Swanson Marine Reserve provides an area where fishing pressure on gag is reduced, as fish species that form spawning aggregations are more susceptible to overexploitation (Coleman et al. 1996; Koenig et al. 2000). However, the results presented in section 4 suggest that the Madison Swanson Marine Reserve is also an important area because it is a preferred source region for transport into the shallow waters of the BBR. Therefore, the existence of preferred particle origins near a known spawning aggregation site suggests that this location could have been evolutionarily chosen this area to spawn because it provides gag with the highest chance for their offspring to arrive in nursery environments conducive for their survival. Simple estimates of recruitment indicate that the population of gag originating in this area could still see at least 10 recruits per individual spawning female, even if 99.9% of their released eggs were killed through various processes. This results presented in this study therefore provide, for the first time, a description of mechanisms capable of providing transport from the shelf break to the nearshore portions of the BBR from a fully four-dimensional perspective. In addition, it is the first successful attempt at describing the role of the physical ocean circulation in setting the transport from adult gag spawning grounds to juvenile gag nursery habitats in the BBR.

Acknowledgements

This research was made possible by grants from the BP/The Gulf of Mexico Research Initiative to the Deep-C Consortium, the National Oceanic and Atmospheric Administration's Northern Gulf Institute (12-NGI-33), the NASA/JPL Ocean Vector Winds Science Team (1419699), and by the Office of Naval Research contract N00014-09-1-0587. The authors would also like to thank the Florida State University Current Meter Facility for the collection of observational data and to Dr. Ekaterina Maksimova for her help processing this data.

References

Barker, E. 1992. Design of the Navy's multivariate optimum interpolation analysis system. Wea. Forecasting, *7*, 2, 220—231.

Barth, A., A. Alvera-Azàrate, and R. H. Weisberg. 2008. A nested model study of the loop current generated variability and its impact on the West Florida Shelf. J. Geophys. Res., *113*, C05009.

Barth, A., A. Alvera-Azàrate, and R. H. Weisberg. 2007. Benefit of nesting a regional model into a large-scale ocean model instead of climatology: Application to the West Florida Shelf. Cont. Shelf. Res., *28*, 561—573.

Beckman, A., and D. Haidvogel. 1993. Numerical simulation of flow around a tall isolated seamount. Part I: problem formulation and model accuracy. J. of Phys. Oceanogr, *23*, 1736—1753.

Bleck, R. 2002. An oceanic general circulation model framed in hybrid isopycnic-Cartesian coordinates. Ocean Modeling, *37*, 55—88

Carlson, P.R., L.A. Yarbro, K.A. Kaufman, and R.A. Mattson. 2010. Vulnerability and resilience of seagrasses to hurricane and runoff impacts along Florida's West coast. Hydrobiologia, *649*, 39—53.

Castelao, R.M. and J.A. Barth. 2005. The relative importance of wind strength and along-shelf bathymetric variations on the separation of a coastal upwelling jet. J. of Phys. Oceanogr., *36*, 412—425.

Chambers, R.C. and E.A. Trippel. 1997. Early Life History and Recruitment in Fish Populations. Springer Publish., 632pp.

Chapman, D.C. 1985. Numerical treatment of cross-shelf open boundaries in a barotropic coastal ocean model. J. of Phys. Oceanogr., *15*, pp. 1060–1075.

Chassignet, E.P., H.E. Hurlburt, O.M. Smedstad, G.R. Halliwell, P.J. Hogan, A.J. Wallcraft, R. Baraille, and R. Bleck. 2007. The HYCOM (HYbrid Coordinate Ocean Model) Data Assimilative System. J. of Mar. Systems, *65*, 60—83.

Chassignet E.P., H.E. Hurlburt, E.J. Metzger, O.M. Smedstad, J. Cummings, G.R. Halliwell, R. Bleck, R. Baraille, A.J. Wallcraft, C. Lozano, H.L. Tolman, A. Srinivasan, S. Hankin, P. Cornillon, R. Weisberg, A. Barth, R. He, F. Werner, and J. Wilkin. 2009. U.S. GODAE: Global ocean prediction with the HYbrid Coordinate Ocean Model (HYCOM). Oceanography, *22*(2), 64–75.

Chassignet, E.P. 2011. Isopycnic and hybrid ocean modeling in the context of GODAE, *in* Operational Oceanography in the 21st Century, A. Schiller and G. Brassington, Eds., Springer, 263—294.

Clark, A.J. and K.H. Brink. 1985. The response of stratified, frictional flow of shelf and slope waters to fluctuating large-scale, low-frequency wind forcing. J. of Phys. Oceanogr., *15*, 439—453.

Coleman, F.C., C.C. Koenig, and L.A. Collins. 1996. Reproductive styles of shallow-water groupers (Pisces: Serranidae) in the eastern Gulf of Mexico and the consequences of fishing spawning aggregations. Environmental Biology of Fishes, *47*, 129—141.

Coleman, F.C., W.F. Figueira, J.S. Ueland, and L.B. Crowder. 2004. The impact of United States recreational fisheries on marine fish populations. Science, *305*, 1958—1960.

Continental Shelf Associates, Inc. 1997. Assessment of hurricane damage in the Florida Big Bend seagrass beds. A final report by Continental Shelf Associates, Inc. submitted to the Mineral Management Service, New Orleans, LA. Contract No. 14-12-0001-30188.

Emery, W.J. and R.E. Thompson. 2001. Data Analysis Methods in Physical Oceanography, 2nd ed. Elsevier Science, 654pp.

Fairall, C.W., E. F. Bradley, J. E. Hare, A. A. Grachev, and J. B. Edson. 2003. Bulk parameterization of air-sea fluxes: updates and verification for the COARE algorithm. J. of Climate, *16*, 571—591.

Flather, R.A. 1976. A tidal model of the northwest European continental shelf, Memoires de la Societe Royale des Sciences de Liege, *6*, 10 141—10 164.

Fitzhugh, G.R., C.C. Koenig, F.C. Coleman, C.B. Grimes., and W Sturges. 2005. Spatial and temporal patterns in fertilization and settlement of young gag (*Mycteroperca microlepis*) along the West Florida shelf. Bull. of Marine Sci., *77*(3), 337—396.

Gentemann, C.L. and Coauthors. 2009. MISST: The multi-sensor improved sea surface temperature project. Oceanography, *22*(3), 76—87

Gentner, B. 2009. Allocation analysis of the Gulf of Mexico gag and red grouper fisheries. Tech. Rep., Gentner Consulting Group, Coastal Conservation Association, 27pp.

Gilbes, F., C. Tomas, J. J. Walsh, and F. E. Mijller-Karger. 1996. An episodic chlorophyll plume on the West Florida Shelf. Cont. Shelf Res., *16*(9), 1201—1224.

Goerss, J.S., and P.A. Phoebus. 1992. The Navy's operational atmospheric analysis. Wea. and Forecast., *7*, 232—249.

Gouillon, F., S.L. Morey, D.S. Dukhovskoy, and J.J. O'Brien. 2010. Forced tidal response in the Gulf of Mexico. J. Geophys. Res., *115*, 1—16.

Haney. 1991. On the pressure gradient force over steep topography in sigma coordinate ocean models. J. of Phys. Oceanogr., *21*, 610—619.

He, R. and R.H. Weisberg. 2002a. Tides on the West Florida shelf. J. of Phys. Oceanogr., *33*, 465-477.

He, R. and R.H. Weisberg. 2002b. West Florida shelf circulation and temperature budget for the 1999 spring transition. Cont. Shelf Res., *22*, 719—748.

He, R. and R.H. Weisberg. 2003. A Loop Current intrusion case study on the West Florida shelf. J. Phys. Oceanogr., *33*, 465—477.

Hetland, R.D., Y. Hsueh, R.R. Lebe, and P.P. Niiler. 1999. A loop current-induced jet along the edge of the West Florida Shelf. Geophys. Res. Letters, *26*(15), 2239—2242.

Hodur, R.M. 1996. The Naval Research Laboratory's Coupled Ocean/Atmosphere Mesoscale Prediction System (COAMPS). Mon. Wea. Rev., *125*, 1414—1430.

Hogan, T. F., and T. E. Rosmond. 1991. The description of the U.S. Navy Operational Global Atmospheric Prediction System’s spectral forecast model. Mon. Wea. Rev., *119*, 1786–1815.

Hood, P.B. and R.A. Schlieder. 1992. Age, growth, and reproduction of gag, *Mycteroperca microlepis* (Pisces: Serranidae), in the eastern Gulf of Mexico. Bull. of Marine Sci., *51*, 337—352.

Iverson, R.L. and H.F. Bittaker. 1986. Seagrass distribution and abundance in eastern Gulf of Mexico coastal waters. Estuarine, Coastal and Shelf Sci., *22*, 577—602.

Kantha, L.H., and C.A. Clayson. 1994. An improved mixed layer model for geophysical applications. J. Geophys. Res., *99*, 25235–25266.

Keener,P., G.D. Johnson, B.W. Stender, E.B. Brothers, and H.R. Beatty. 1988. Ingress of postlarval gag *Mycteroperca microlepis* (Pisces: Serranidae), through a South Carolina barrier island inlet. Bull. of Marine Sci., *42*, 376—396.

Kennedy, A.J., M.L. Griffin, S.L. Morey, S.R. Smith, and J.J. O'Brien. 2007. Effects of El Niño—Southern Oscillation on sea level anomalies along the Gulf of Mexico coast. J. Geophys. Res., *112*, C05047, doi:10.1029/2006JC003904.

Koenig, C.C. and F.C. Coleman. 1998. Absolute abundance and survival of juvenile gags in sea grass beds of the northeastern Gulf of Mexico. Trans. of the American Fisheries Soc., *128*, 44—55.

Koenig, C.C., F.C. Coleman, C.B. Grimes, G.R. Fitzhugh, K.M. Scanlon, C.T. Gledhill, and M. Grace. 2000. Protection of fish spawning habitat for the conservation of warm temperate reef fish fisheries of shelf-edge reefs of Florida. Bull. of Marine Sci., *66*, 593—616

Liu, W.T., and W. Tang. 1996. Equivalent neutral wind. JPL Publ., 96-17, 16pp.

Maksimova, E. and A.J. Clarke. 2013. Multiyear subinertial and seasonal Eulerian current observations near the Florida Big Bend coast. J. Phys. Oceanogr. doi:10.1175/JPO-D-12-0135.1, *in press*

Marchesiello, P., J. McWilliams, and A. Shchepetkin. 2001. Open boundary condition for long-term integration of regional oceanic models. Ocean Modell., *3*, 1—20

Marmorino, G.O. 1983a. Summertime coastal currents in the northeastern Gulf of Mexico, J. Phys. Oceanogr., *13*, 65—77

Marmorino, G.O. 1983b. Variability of current, temperature, and bottom pressure across the West Florida continental shelf, Winter 1981-1982, J. Geophys. Res., *8*, C7 4439—4457

Mellor, G., and T. Yamada. 1982. Development of a turbulence closure model for geophysical fluid problems. Reviews of Geophysics and Space Physics, *20*, 851—875.

Mellor, G., and T. Yamada. 1974. A hierarchy of turbulence closure models for planetary boundary layers. J. of Atmos Science, *31*, 1791—1806.

Mesinger, F. and Coauthors. 2006. North American Regional Reanalysis. Bull. Am. Met. Soc., *87*, 3, 343—360.

Mitchum, G.T. and A.J. Clarke. 1986. Evaluation of frictional, wind-forced long-wave theory on the West Florida shelf. J. of Phys. Oceanogr., *16*, 1029—1037.

Mitchum, G.T. and W. Sturges. 1982. Wind-driven currents on the West Florida Shelf. J. of Phys. Oceanogr., *12*, 1310—1317.

Lentz, S., 2012: Buoyant coastal currents. *Buoyancy-Driven Flows*, E. Chassginet, C. Cenedese, and J. Verron, Eds., Cambridge Univ. Press, 164—202.

Morey, S.L., D. S. Dukhovskoy, and M.A. Bourassa. 2009. Connectivity of the Apalachicola River flow variability and the physical and bio-optical oceanic properties of the northern West Florida Shelf. Cont. Shelf Res., *29*, 1264—1275.

Morey, S.L., J. Zavala-Hidalgo, and J.J. O'Brien. 2005. The seasonal variability of continental shelf circulation in the northern and western Gulf of Mexico from a high-resolution numerical model, *in* Circulation in the Gulf of Mexico: Observations and Models, *Geophys. Monogr.*, No. 161, Amer. Geophys. Union, 203—218.

Morey, S.L., and J.J. O'Brien. 2002. The spring transition from horizontal to vertical thermal stratification on a midlatitude continental shelf. J. of Geophys. Res., *29*, 1264—1275.

Norcross, B.L. and R.F. Shaw. 1984. Oceanic and estuarine transport of fish eggs and larvae: a review. Trans. of the American Fisheries Soc., *113*, 155—165.

North, E. W., Z. Schlag, R. R. Hood, M. Li, L. Zhong, T. Gross, and V. S. Kennedy. 2008. Vertical swimming behavior influences the dispersal of simulated oyster larvae in a coupled particle-tracking and hydrodynamic model of Chesapeake Bay. Marine Ecology Progress Series, *359*, 99—115.

Pedlosky, J. 1986. Geophysical Fluid Dynamics, 2nd ed. Springer-Verlag, 710pp.

Rosmond, T.E. 1992. The design and testing of the Navy Operational Global Atmospheric Prediction System. Weather and Forecasting, *7*, 262—272.

Rothschild, B.J. 1986. Dynamics of Marine Fish Populations. Harvard University Press, 277pp.

Rothschild, B.J. and T.R. Osborn. 1988. Small-scale turbulence and plankton contact rates. J. of Plankton Res., *10*, 465—474.

Saha, S., and Coauthors. 2006. The NCEP Climate Forecast System. J. Climate, *19*, 3483—3517.

Schlag, Z., E. W. North, and K. Smith. 2008. Larval TRANSport Lagrangian model (LTRANS) User's Guide. University of Maryland Center for Environmental Science, Horn Point Laboratory, Cambridge, MD, 146 pp.

Shchepetkin, A.F. and J.C. McWilliams. 2005. The regional oceanic modeling system (roms): a split-explicit, free-surface, topography-following-coordinate oceanic model. Ocean Modelling, *9*, 147—404.

Shchepetkin, A.F. and J.C. McWilliams. 2003. A method for computing horizontal pressure-gradient force in an oceanic model with a nonaligned vertical coordinate. J. of Geophys. Res., *108*, 3090.

Shchepetkin, A.F. and J.C McWilliams. 1998. Quasi-monotone advection schemes based on explicit locally adaptive dissipation. Mon. Wea. Rev., *126*, 1541—1580.

Sikiric, M.D., I. Janekovic, M. Kuzmic. 2009. A new approach to bathymetry smoothing in sigma-coordinate ocean models. Ocean Modelling, *29*, 128—136.

Smith, S. R., P. M. Green, A. P. Leonardi, and J. J. O'Brien. 1998. Role of multiple-level tropospheric circulations in forcing ENSO winter precipitation anomalies. Mon. Weather Rev., *126*, 3102—3116.

Smolarkiewicz, P. K. 1984. A fully multidimensional positive definite advection transport algorithm with small implicit diffusion. J. Comput. Phys., *54*, 325—362.

Thompson, M.J. and N.W. Phillips. 1987. *See Continental Shelf Associates, Inc., 1997*.

Weatherly, G.L. and D. Thistle. 1997. On the wintertime currents of the Florida Big Bend region. Cont. Shelf Res., *17*, 11 1297—11 1319.

Weisberg, R.H., R. He, Y. Liu, and J.I. Virmani. 2005. West Florida shelf circulation on synoptic, seasonal, and interannual time scales, *in* Circulation in the Gulf of Mexico: Observations and Models, Geophys. Monogr., No. 161, Amer. Geophys. Union, 325—347.

Weisberg, R.H. and R. He. 2003. Local and deep-ocean forcing contributions to anomalous water properties on the West Florida Shelf. J. Geophys. Res., *108*(C6), 3184.

Weisberg, R.H., Z. Li and F. Muller-Karger. 2001. West Florida shelf response to local wind forcing: April 1998. J. Geophys. Res., *106*(C12), 31 239—31 262.

Werner, F.E., J.A. Quinlan, B.O. Blanton, R.A. Luettich Jr.. 1997. The role of hydrodynamics in explaining variability in fish populations. J. of Sea Res., *37*, 195—212.

Yang, H. and R.H. Weisberg. 1999. Response of the West Florida Shelf circulation to climatological wind stress forcing. J. Geophys. Res., *104*(C3), 5301—5320.

Yang, H., R.H. Weisberg, P.P. Niiler, W. Sturges, and W. Johnson. 1999. Lagrangian circulation and the forbidden zone on the West Florida Shelf. Cont. Shelf Res., *19*, 1221—1245.

Tables

Table 1: Atmospheric model grid specifications

Model	Grid Spacing	Temporal Resolution	Range
CFSR	T382	1 hour	1979 – 2009
COAMPS	0.2°x0.2°	3 hour	2003 – present
NARR	~32.46 km	3 hour	1979 – present
NOGAPS	0.5°x0.5°	3 hour	2003 – present

Table 2: Linear regression fits for wind speeds from each atmospheric dataset nearest buoys 42036 and 42039, and tower SGOF1 to observed wind speeds at each location. Winds have been low-passed filtered using a cosine-Lanczos filter that passes 10% power at frequency 2π/30 hrs. All correlations are statistically significant at the 95% confidence interval.

Atmospheric Forcing	Location	Slope	Intercept	R^2
CFSR	42036	0.7706	0.5225	0.9016
	42039	0.9521	0.1760	0.9291
	SGOF1	0.9939	0.0503	0.9321
COAMPS	42036	0.7462	0.7335	0.8244
	42039	0.8979	0.5071	0.8764
	SGOF1	0.9234	0.3516	0.8732
NARR	42036	0.7062	-0.0038	0.8067
	42039	0.7773	0.1873	0.8120
	SGOF1	0.8154	0.0381	0.8443
NOGAPS	42036	0.8090	0.5187	0.8510
	42039	0.8867	0.6093	0.9042
	SGOF1	0.9867	0.1355	0.8920

Table 3: Linear regression fits for SST between ocean model runs and moored observations

Atmospheric Forcing	Location	Slope	Intercept	R^2
CFSR	42036	1.0021	-0.1610	0.9722
	42039	1.0178	-0.1557	0.9516
	SGOF1	1.0173	-0.6935	0.9829
COAMPS	42036	1.0571	-1.2039	0.9596
	42039	1.0821	-1.4694	0.9394
	SGOF1	1.0436	-0.7526	0.9785
NARR	42036	1.0234	-0.8640	0.9719
	42039	1.0264	-0.5442	0.9547
	SGOF1	1.0278	-1.4483	0.9796
NOGAPS	42036	1.0180	-0.2467	0.9624
	42039	1.0359	-0.3620	0.9396
	SGOF1	0.9930	0.3611	0.9751

Figures

Figure 1: Florida Big Bend and the BBROMS modeling domain. Triangles represent observational towers, open circles represent NDBC buoys, closed circles represent coastal sea level stations, dots depict particle seeding locations, and the star denotes the location of the current profiler at site S.

Figure 2: Wind stress roses for 2004—2010 spring months (Feb—May), calculated from each of the BBROMS simulations. The atmospheric product used to force each ocean model simulation is indicated above the four roses. Bars point in the direction from which the wind originates, and the lengths of the bars indicate the percentage of time that winds come from each direction. Different colors represent the range of wind stress magnitudes.

Figure 3: Power spectral density (N^2m^4s) for alongshore subinertial wind stress estimated using the maximum entropy method. Winds are extracted from a point near buoy 42036 and rotated 30 degrees west of North.

Figure 4: Modeled and observed springtime sub-inertial sea level anomalies near Panama City, FL. Observations are shown in pink, CFSR-forced BBROMS in red, COAMPS-forced BBROMS in green, NARR-forced BBROMS in blue, and NOGAPS-forced BBROMS in black.

Figure 5: Annual mean sea surface temperatures (°C) averaged across the portion of the BBROMS domain that is covered by the 9km MISST.

Figure 6: Modeled and observed depth-averaged springtime alongshore currents at site N7. Values in the triplet indicate the correlation R, regression slope, and difference between modeled mean and observed mean currents.

Figure 7: Same as Fig, 6, except for depth-averaged springtime cross-shore currents at site N7.

Figure 8: Modeled and observed current profiles at site N7, averaged for the period Feb—June. Dashed lines show the 20th and 80th percentiles of the observed flow, and the interquantile range is the difference between the two percentiles.

Figure 9: Modeled and observed depth-averaged springtime currents at site S. Values in the triplet indicate the correlation R, regression slope, and difference between modeled mean and observed mean currents.

Figure 10: Seven-year mean vertically averaged spring velocities for contemporaneous model runs forced by (a) CFSR, (b) COAMPS, (c) NARR, and (d) NOGAPS. Current speeds are contoured in color and velocity vectors are plotted every 10 gridpoints.

Figure 11: Same as Fig. 10, except for mean near-surface velocities from model runs forced by (a) CFSR, (b) COAMPS, (c) NARR, and (d) NOGAPS.

Figure 12: Same as Fig. 10, except for mean near-bottom velocities from model runs forced by (a) CFSR, (b) COAMPS, (c) NARR, and (d) NOGAPS.

Figure 13: Similar to Fig. 10, except for mean depth-averaged velocities during each spring season for the model forced by CFSR.

Figure 14: Vertically averaged spring velocities for the CFSR-forced BBROMS simulation. Velocities from the seven-years of simulations are conditionally averaged for springtime flow only during (top) winds that range from West to North or (bottom) during winds that range from South to East.

Figure 15: Vertically averaged spring velocities from the CFSR-forced BBROMS simulation. Velocities are conditionally averaged for springtime flow during winds that range either from West to North or from South to East. This figure is the average of each panel in Fig. 14.

Figure 16: The ratio ζ/f for flow during (left) northwesterly winds and during (right) southeasterly winds are plotted in color, calculated from seven-year mean depth-averaged currents. Contours for both f/h and potential vorticity are drawn at $0.046\text{x}10^{-5}$, $0.07\text{x}10^{-5}$, $0.1\text{x}10^{-5}$, $0.145\text{x}10^{-5}$, $0.18\text{x}10^{-5}$, $0.238\text{x}10^{-5}$, $0.295\text{x}10^{-5}$, $0.37\text{x}10^{-5}$, $0.46\text{x}10^{-5}$, and $0.7\text{x}10^{-5}$ $m^{-1}s^{-1}$. Areas with higher magnitudes of ζ/f, or where contours are not aligned, indicate where cross-isobath flow should occur under PV-conserving conditions.

Figure 17: Contours depict the mean change in particle depth from one time step to the next ($\Delta h/h$) at each location, with contour intervals at ± 0.0025, ± 0.005, and every 0.002 from ± 0.01 to ± 0.03. Colors depict the mean change in particle relative vorticity between time steps over the absolute vorticity at the particle location from the previous time step ($\Delta\zeta/(\zeta+f)$).

Figure 18: Particle track density for (a) all particles released over the seven-year advection period (percentage of all 733,824 particles), and (b)—(h) calculated for each year (percentage of 104,832 particles released during that year). Particles are advected in the depth-averaged velocities from the CFSR-forced BBROMS simulation.

Figure 19: (top) Particle track density of all particles that reached the 10m isobath during their advection period and (bottom) the origins of particles that successfully reached the 10m isobath during their advection. Circles are colored by the percentage of successful particles originating from that location, where open circles indicate zero particles to arrive inshore.

Figure 20: Trajectory of a particle released at 15:00 UTC on 11 February 2005. The color of the particle's path indicates the time during the particle's advection to the nearshore region around Apalachicola Bay on 11 March 2005 at 12:00 UTC.

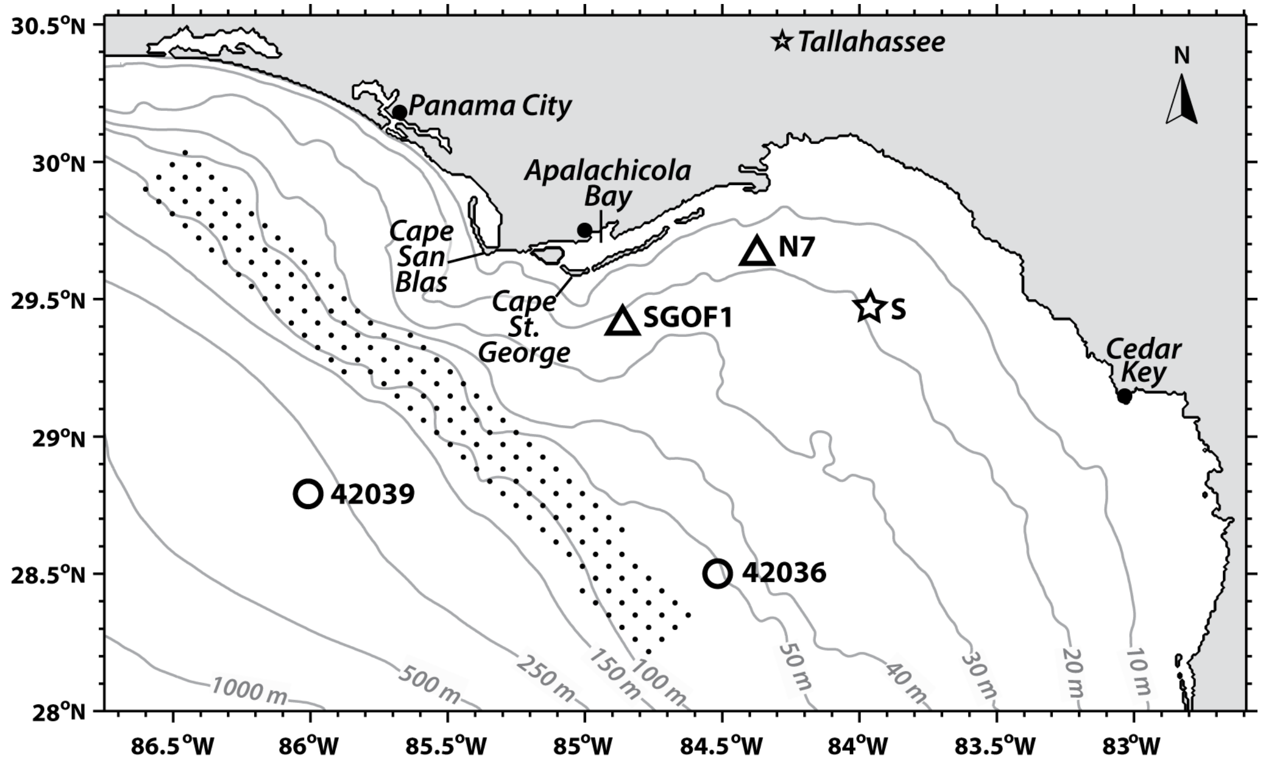

Figure 1: Florida Big Bend and the BBROMS modeling domain. Triangles represent observational towers, open circles represent NDBC buoys, closed circles represent coastal sea level stations, dots depict particle seeding locations, and the star denotes the location of the current profiler at site S.

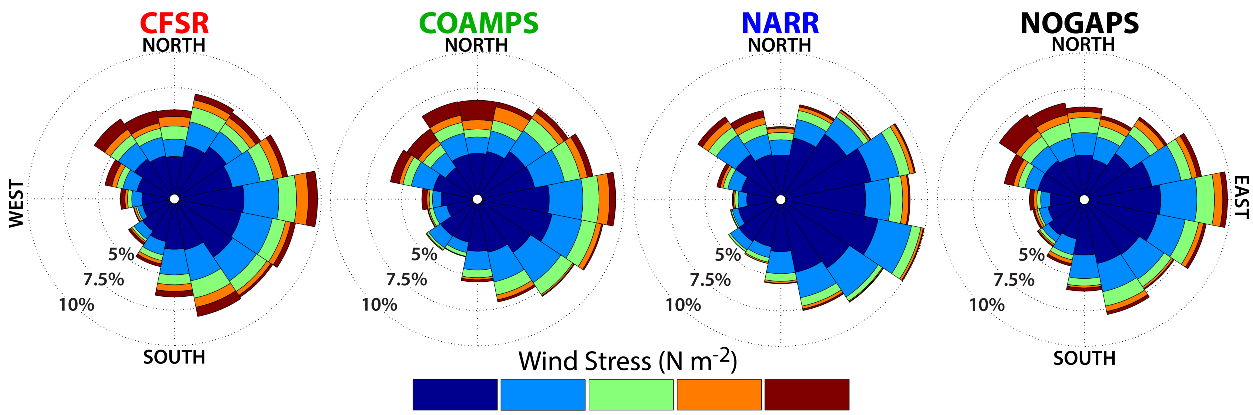

Figure 2: Wind stress roses for 2004—2010 spring months (Feb—May), calculated from each of the BBROMS simulations. The atmospheric product used to force each ocean model simulation is indicated above the four roses. Bars point in the direction from which the wind originates, and the lengths of the bars indicate the percentage of time that winds come from each direction. Different colors represent the range of wind stress magnitudes.

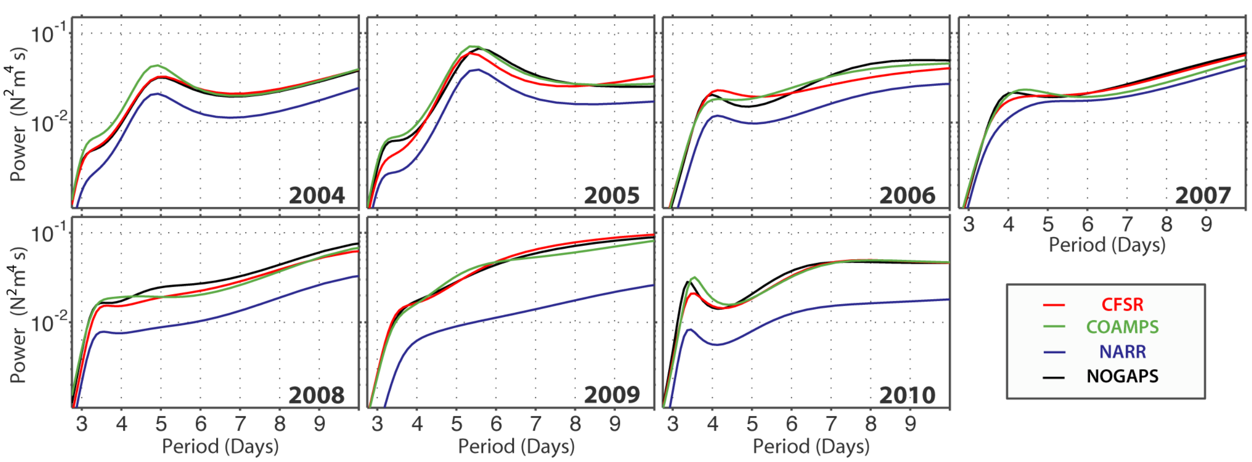

Figure 3: Power spectral density (N^2m^4s) for alongshore subinertial wind stress estimated using the maximum entropy method. Winds are extracted from a point near buoy 42036 and rotated 30 degrees west of North.

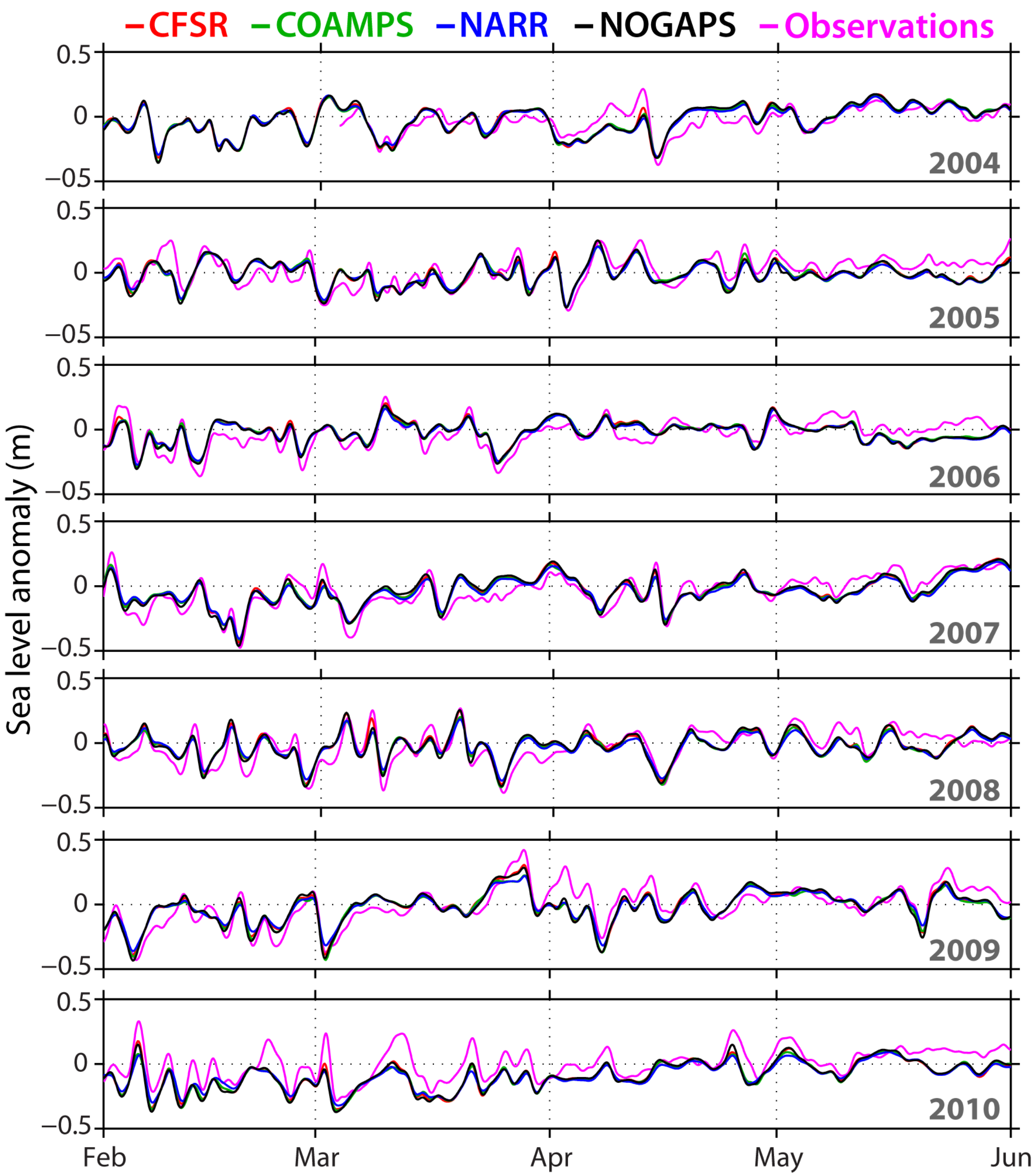

Figure 4: Modeled and observed springtime sub-inertial sea level anomalies near Panama City, FL. Observations are shown in pink, CFSR-forced BBROMS in red, COAMPS-forced BBROMS in green, NARR-forced BBROMS in blue, and NOGAPS-forced BBROMS in black.

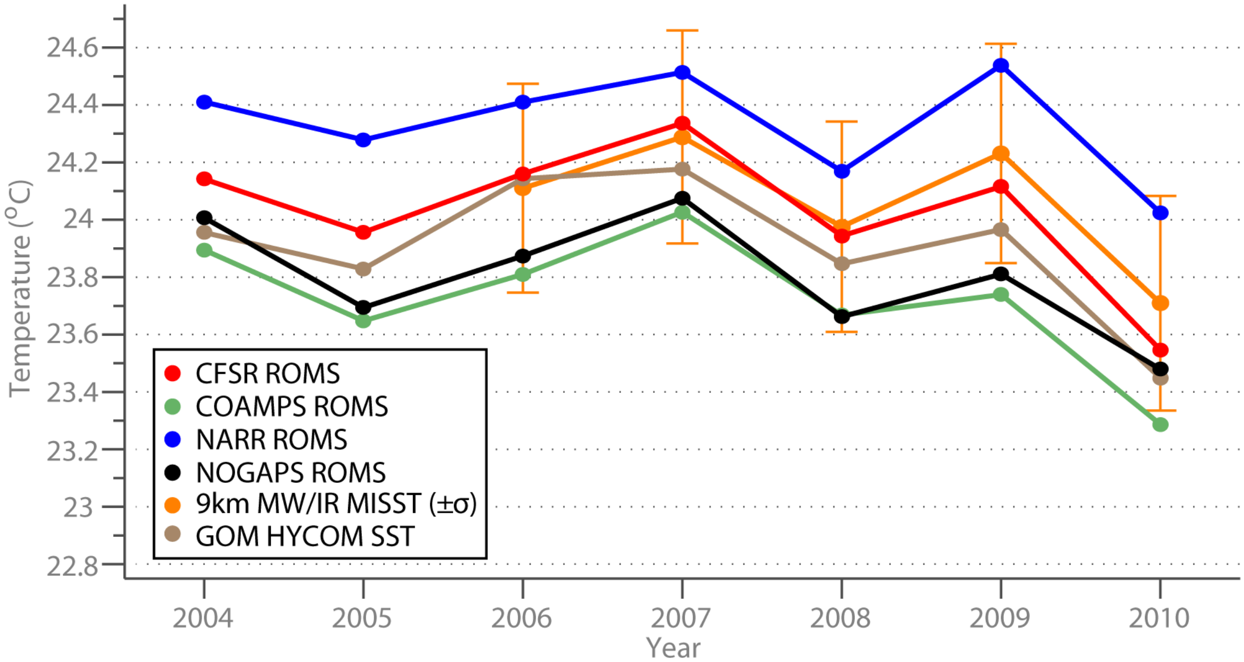

Figure 5: Annual mean sea surface temperatures (°C) averaged across the portion of the BBROMS domain that is covered by the 9km MISST.

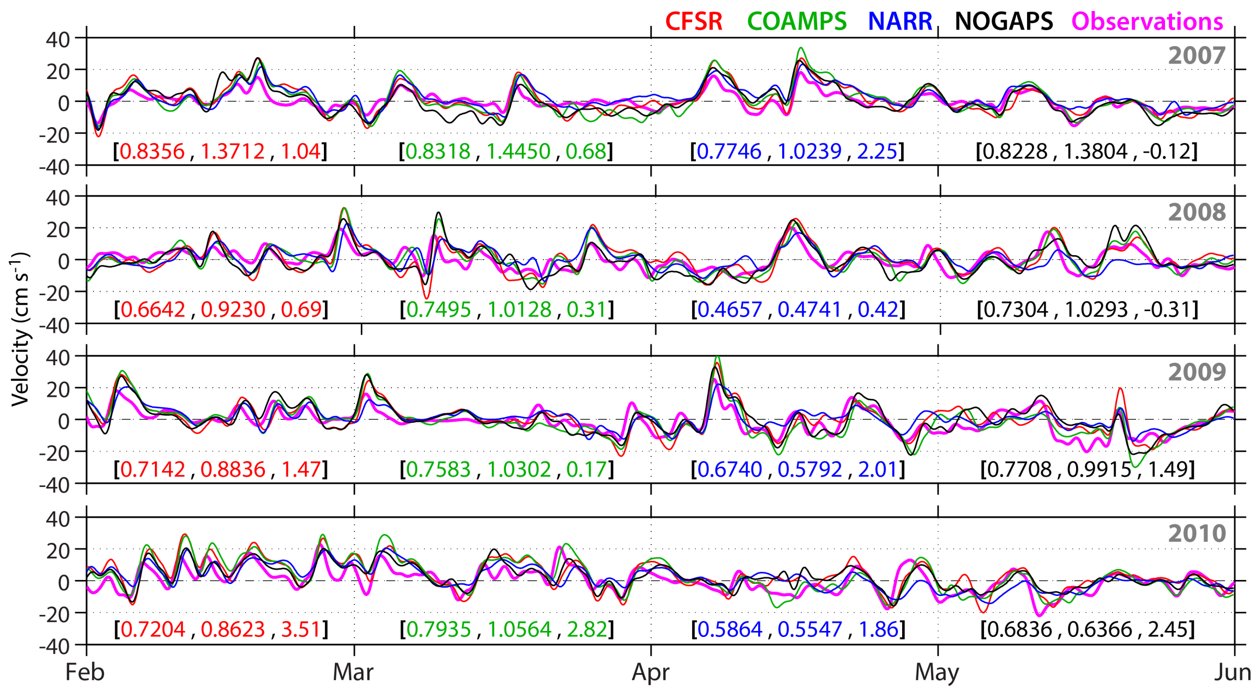

Figure 6: Modeled and observed depth-averaged springtime alongshore currents at site N7. Values in the triplet indicate the correlation R, regression slope, and difference between modeled mean and observed mean currents.

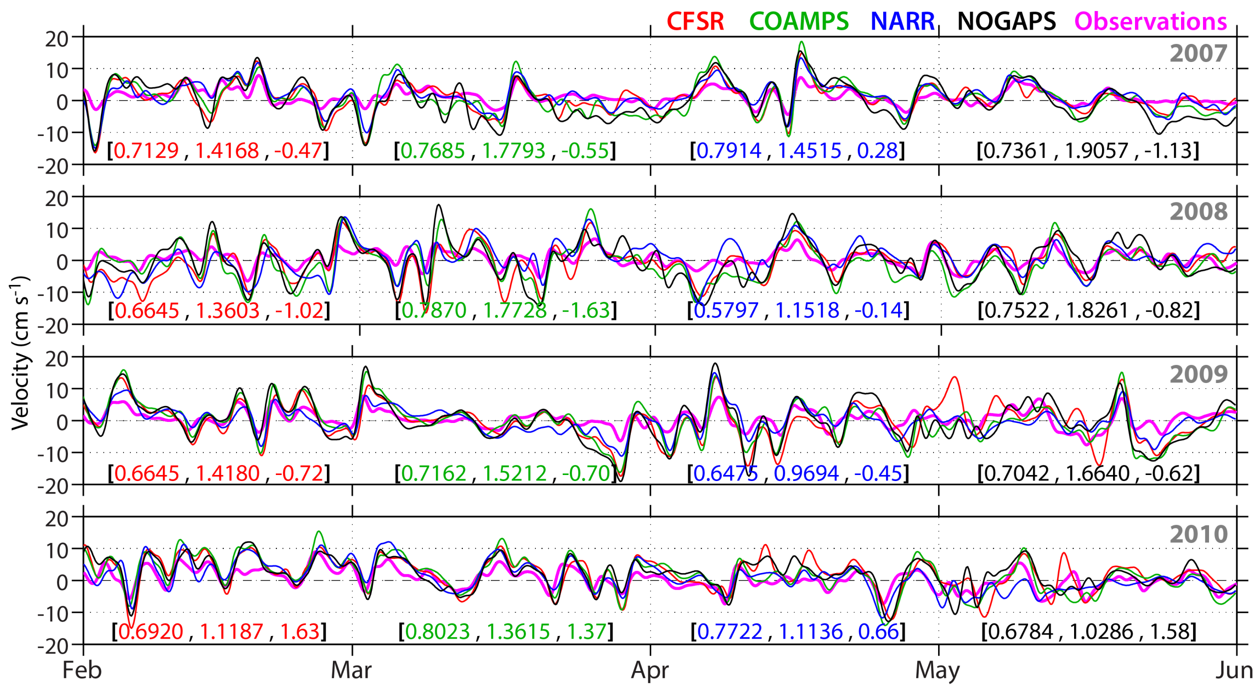

Figure 7: Same as Fig, 6, except for depth-averaged springtime cross-shore currents at site N7.

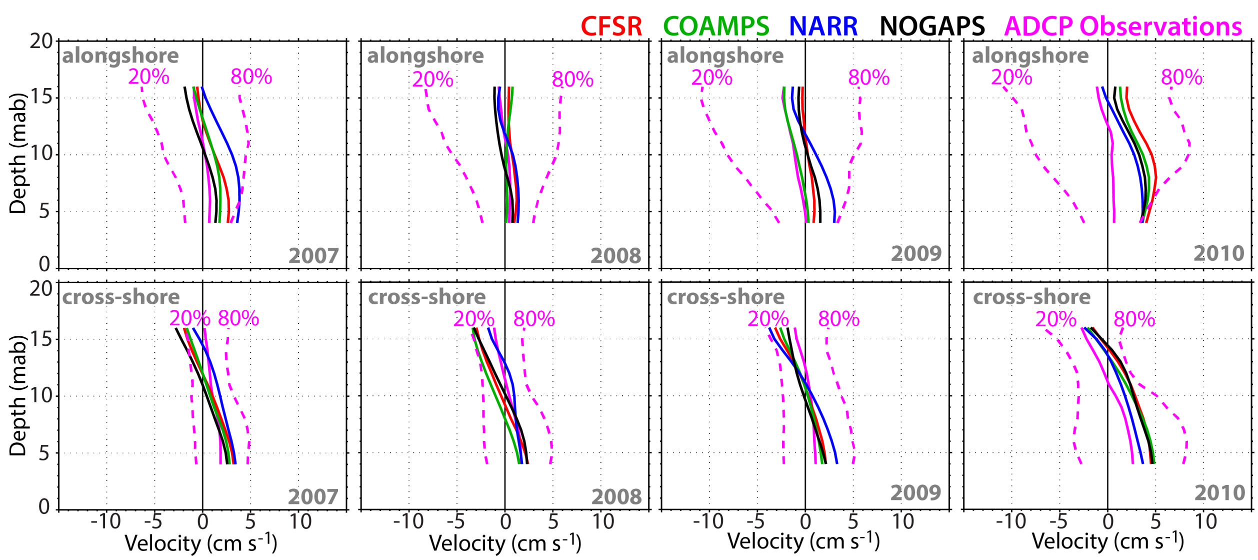

Figure 8: Modeled and observed current profiles at site N7, averaged for the period Feb—June. Dashed lines show the 20th and 80th percentiles of the observed flow, and the interquantile range is the difference between the two percentiles.

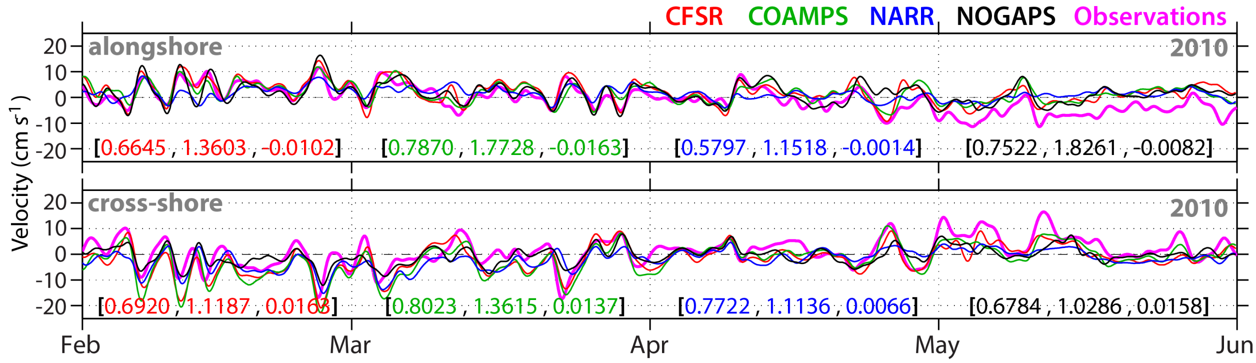

Figure 9: Modeled and observed depth-averaged springtime currents at site S. Values in the triplet indicate the correlation R, regression slope, and difference between modeled mean and observed mean currents.

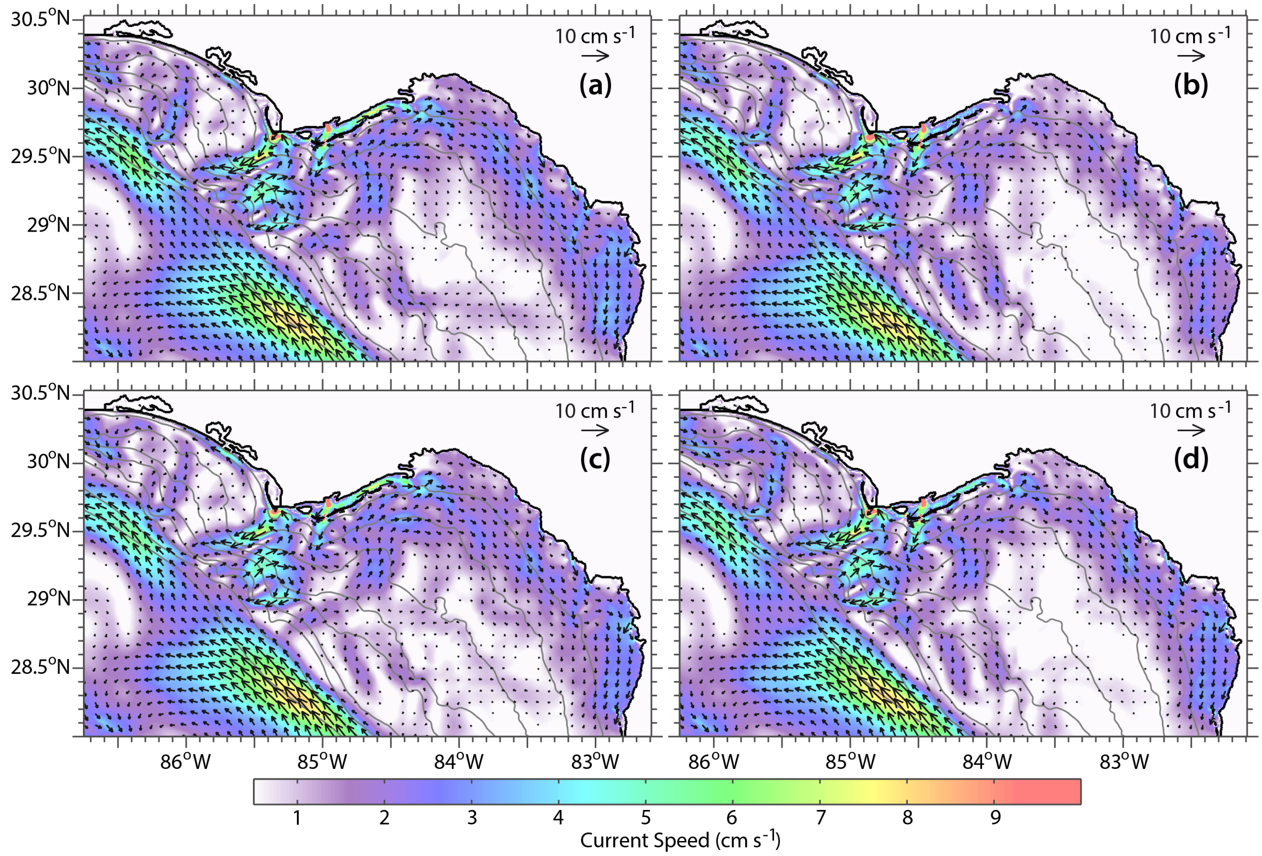

Figure 10: Seven-year mean vertically averaged spring velocities for contemporaneous model runs forced by (a) CFSR, (b) COAMPS, (c) NARR, and (d) NOGAPS. Current speeds are contoured in color and velocity vectors are plotted every 10 gridpoints.

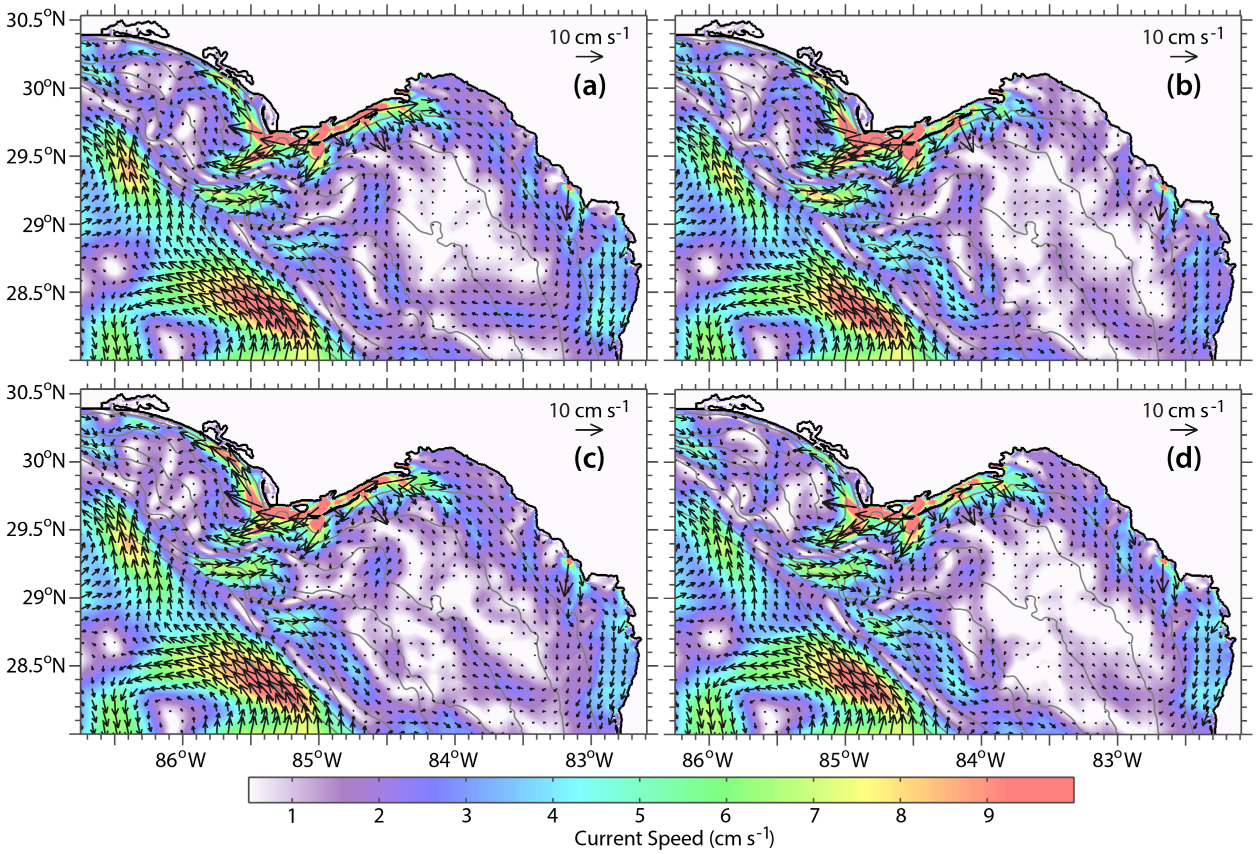

Figure 11: Same as Fig. 10, except for mean near-surface velocities from model runs forced by (a) CFSR, (b) COAMPS, (c) NARR, and (d) NOGAPS.

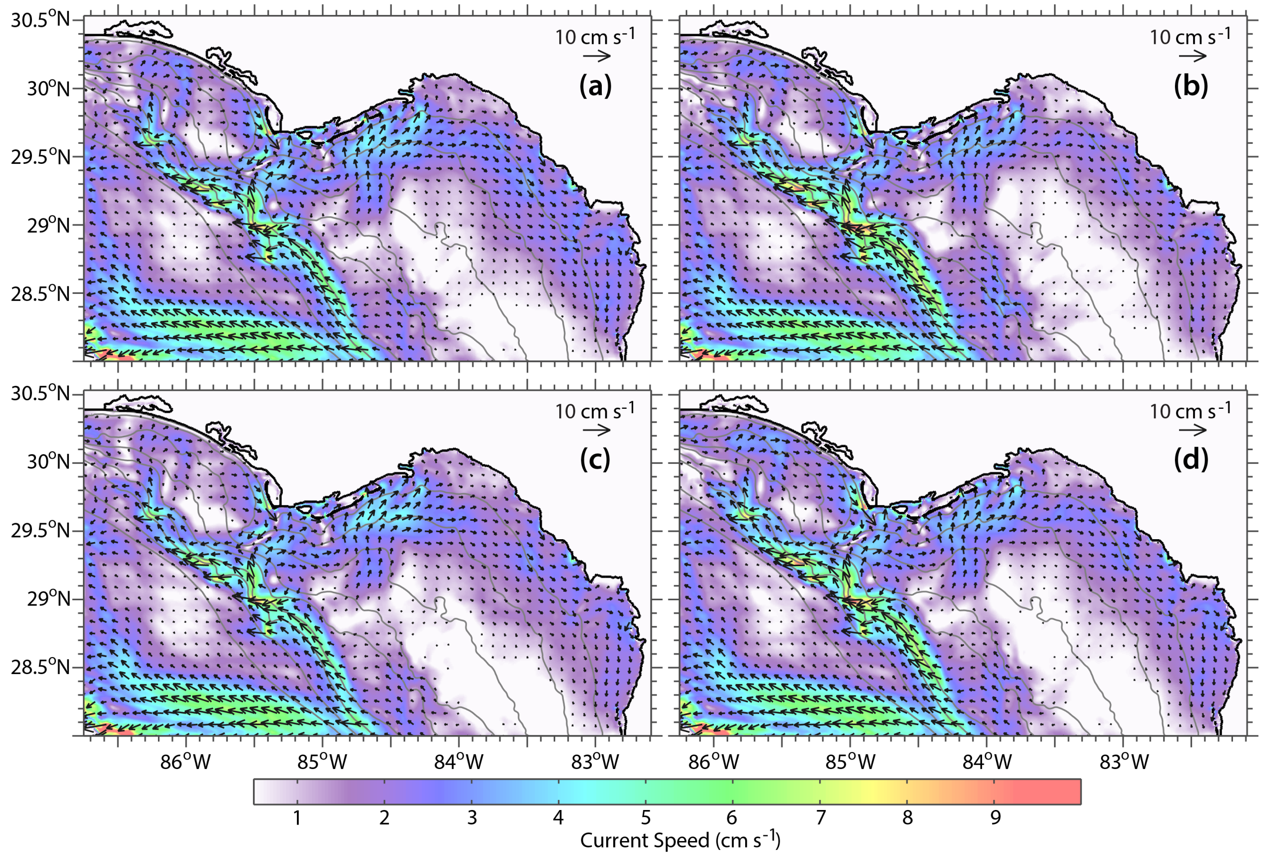

Figure 12: Same as Fig. 10, except for mean near-bottom velocities from model runs forced by (a) CFSR, (b) COAMPS, (c) NARR, and (d) NOGAPS.

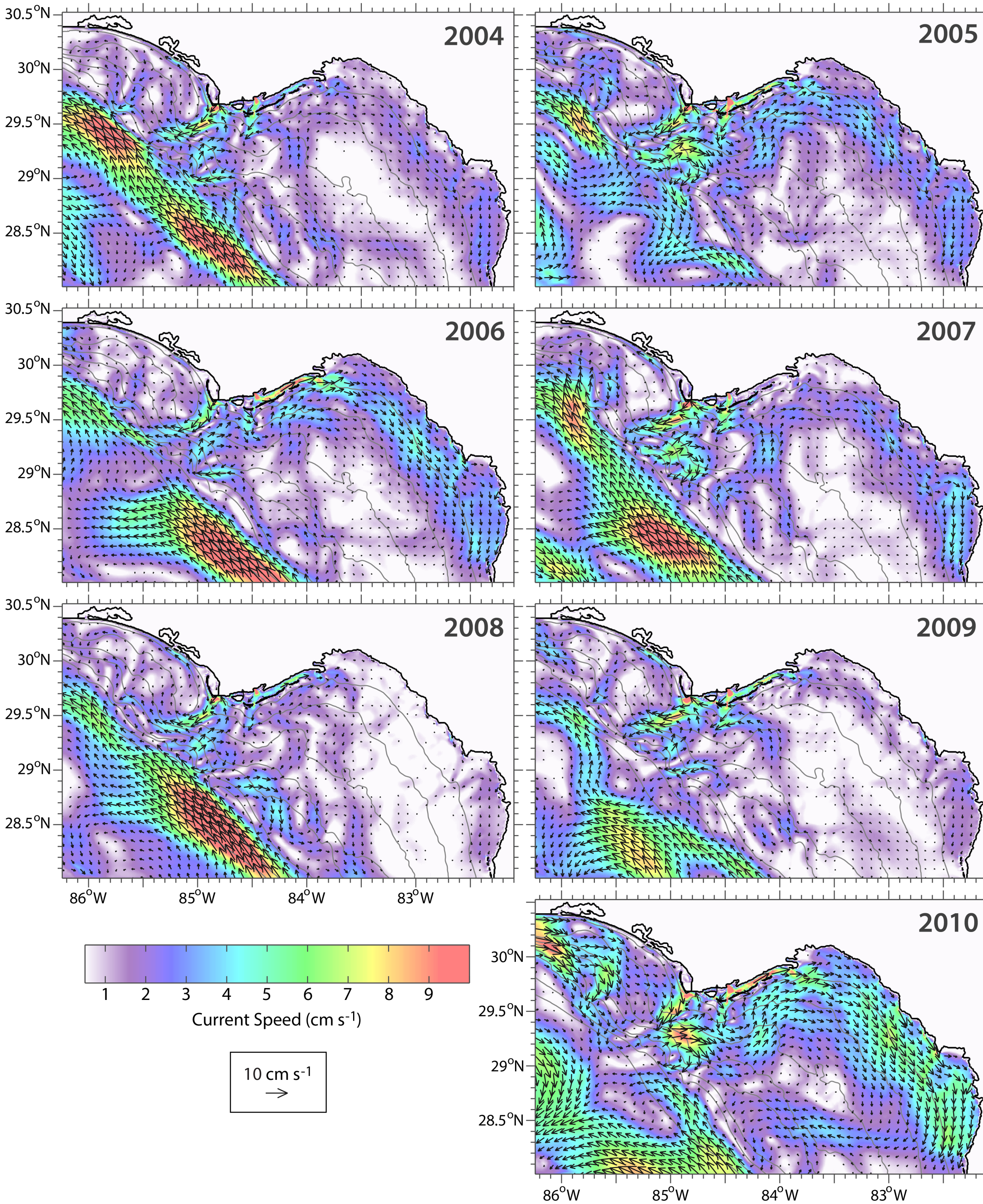

Figure 13: Similar to Fig. 10, except for mean depth-averaged velocities during each spring season for the model run forced by CFSR.

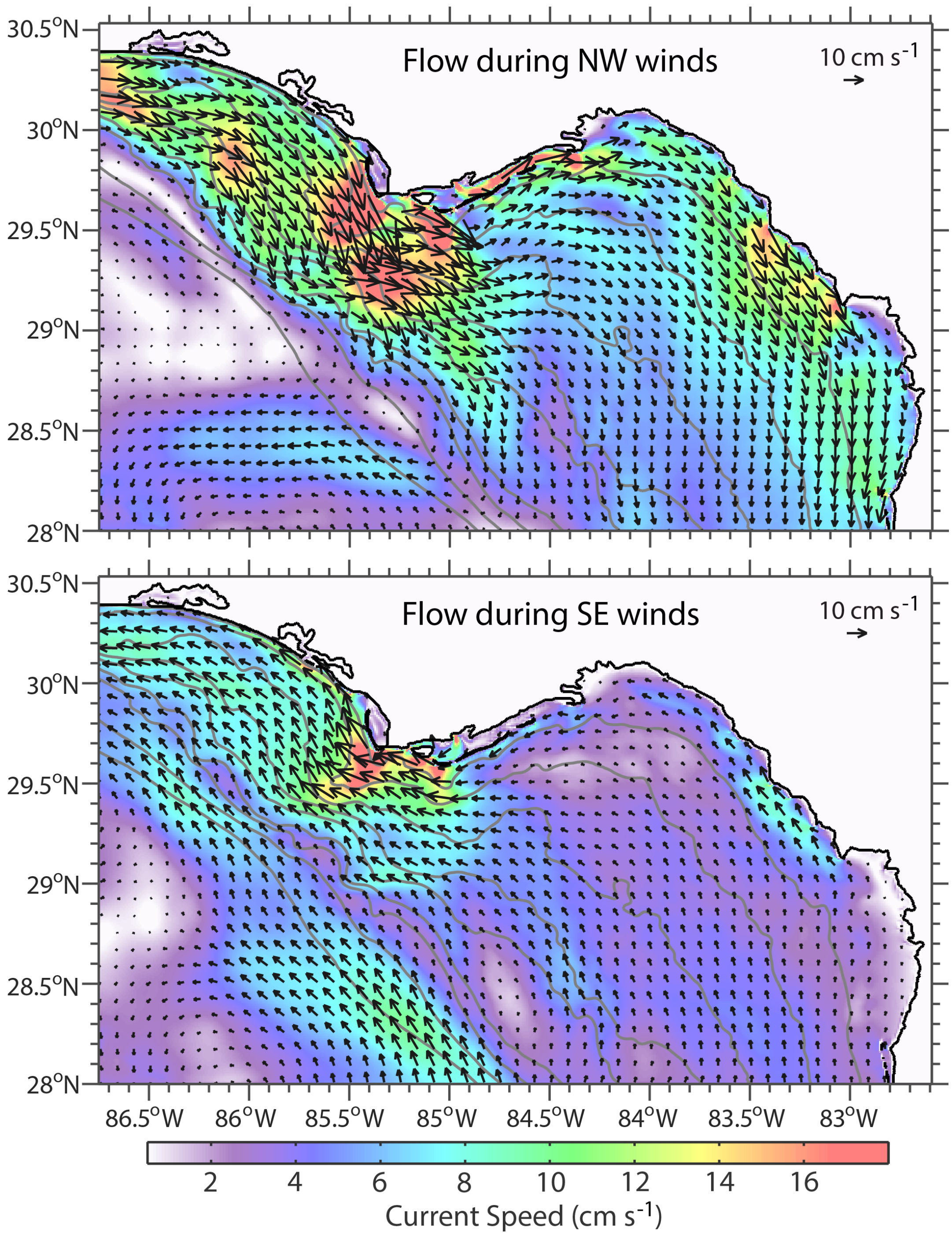

Figure 14: Vertically averaged spring velocities for the CFSR-forced BBROMS simulation. Velocities from the seven-years of simulations are conditionally averaged for springtime flow only during (top) winds that range from West to North or (bottom) during winds that range from South to East.

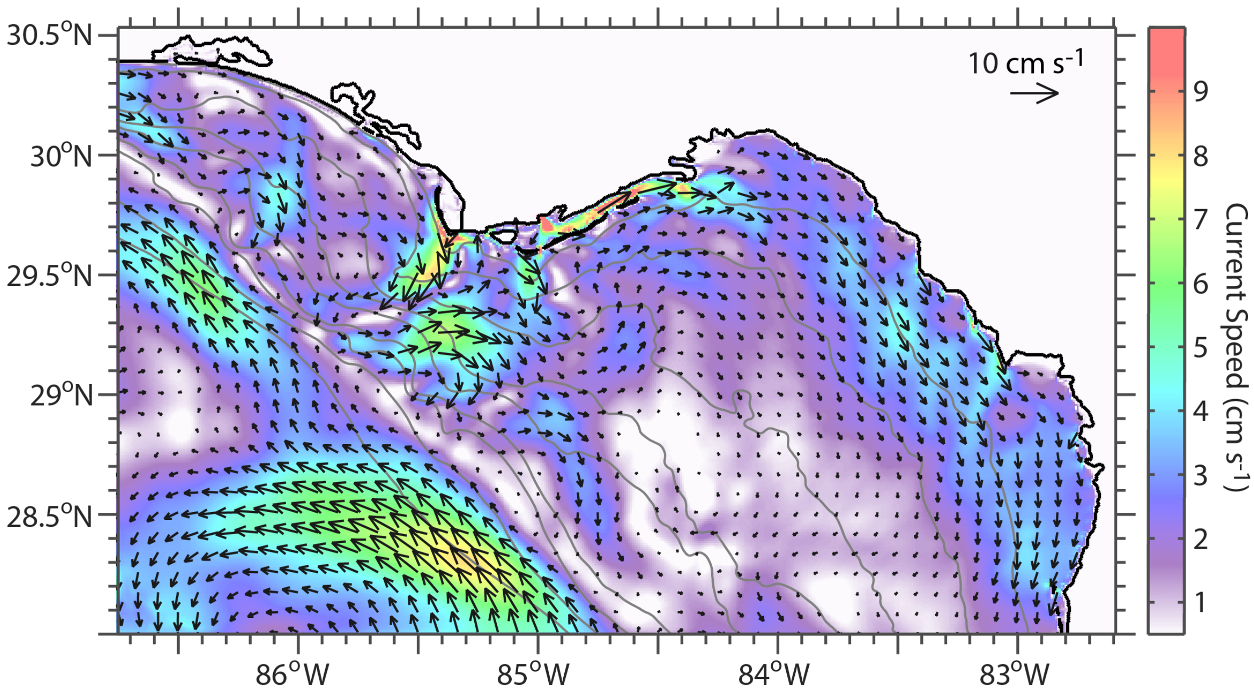

Figure 15: Vertically averaged spring velocities from the CFSR-forced BBROMS simulation. Velocities are conditionally averaged for springtime flow during winds that range either from West to North or from South to East. This figure is the average of each panel in Fig. 14.

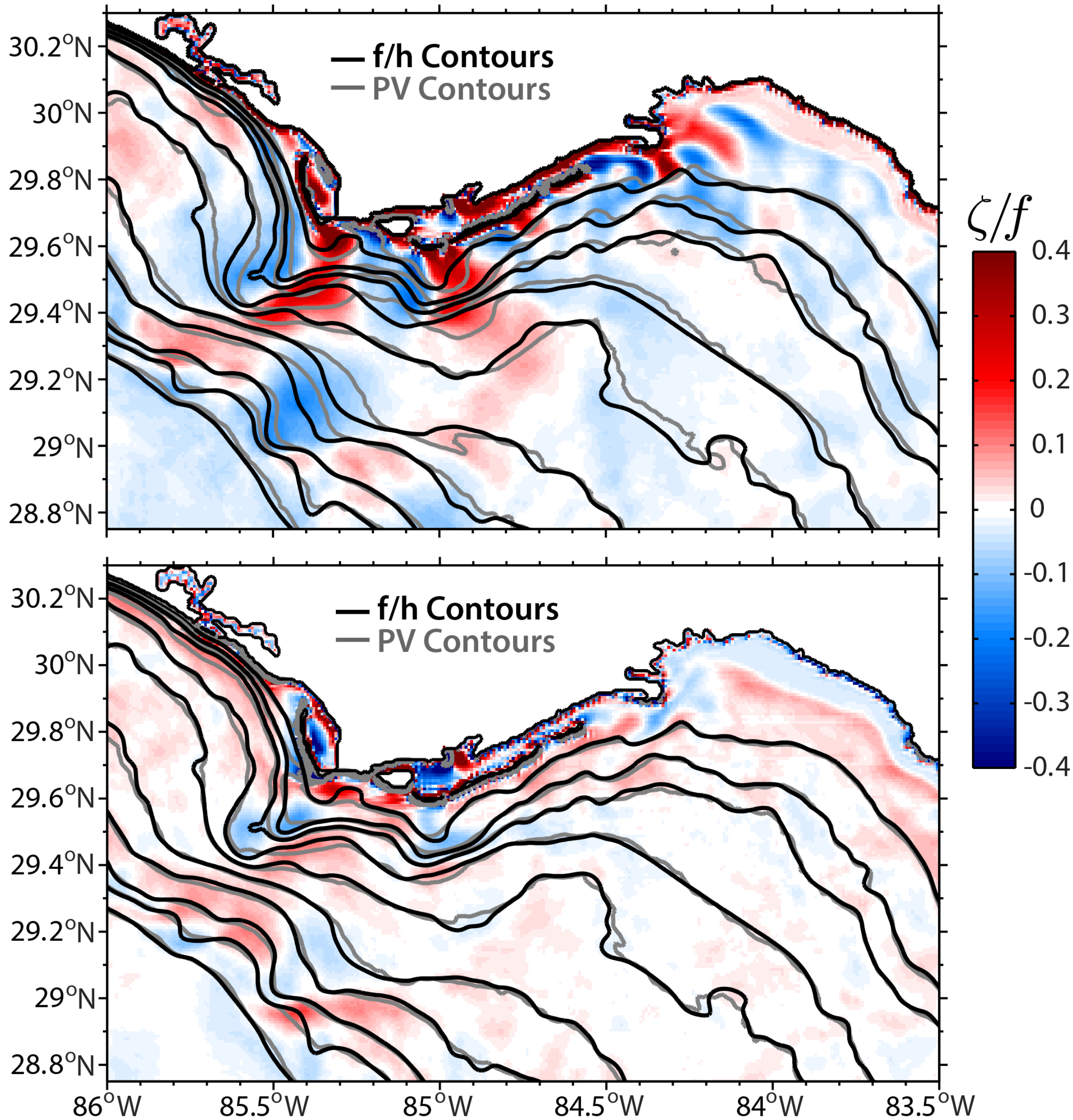

Figure 16: The ratio ζ/f for flow during (left) northwesterly winds and during (right) southeasterly winds are plotted in color, calculated from seven-year mean depth-averaged currents. Contours for both f/h and potential vorticity are drawn at $0.046\text{x}10^{-5}$, $0.07\text{x}10^{-5}$, $0.1\text{x}10^{-5}$, $0.145\text{x}10^{-5}$, $0.18\text{x}10^{-5}$, $0.238\text{x}10^{-5}$, $0.295\text{x}10^{-5}$, $0.37\text{x}10^{-5}$, $0.46\text{x}10^{-5}$, and $0.7\text{x}10^{-5}$ $m^{-1}s^{-1}$. Areas with higher magnitudes of ζ/f, or where contours are not aligned, indicate where cross-isobath flow should occur under PV-conserving conditions.

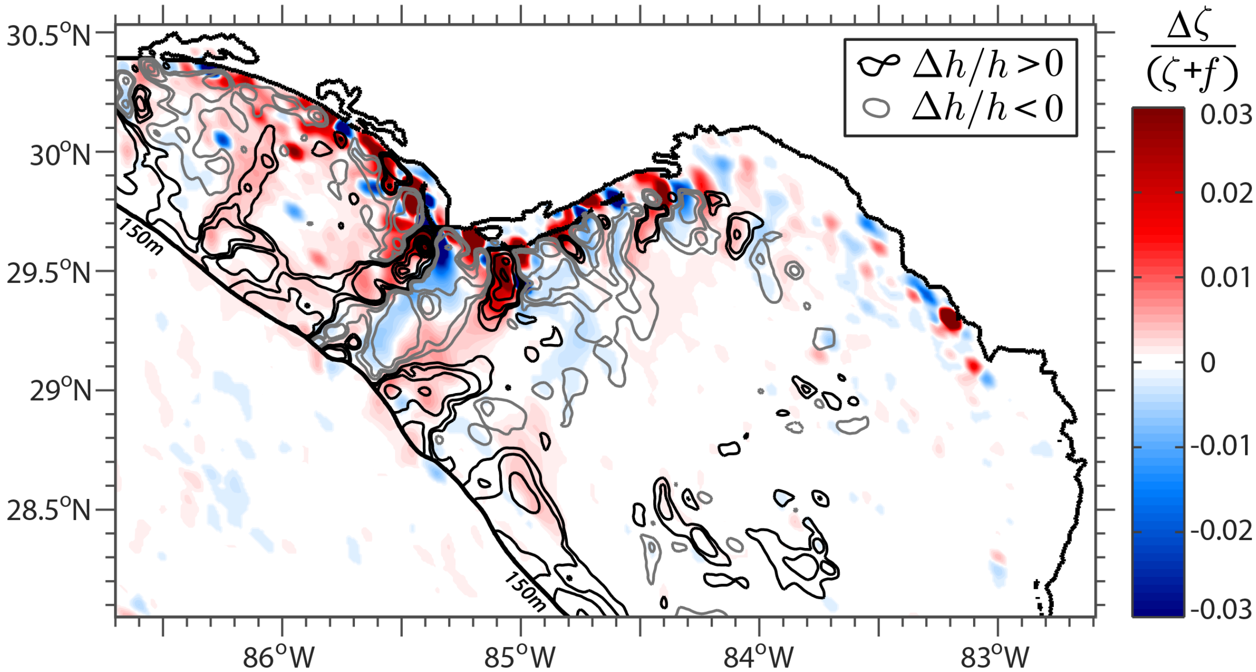

Figure 17: Contours depict the mean change in particle depth from one time step to the next ($\Delta h/h$) at each location, with contour intervals at ± 0.0025, ± 0.005, and every 0.002 from ± 0.01 to ± 0.03. Colors depict the mean change in particle relative vorticity between time steps over the absolute vorticity at the particle location from the previous time step ($\Delta\zeta/(\zeta+f)$).

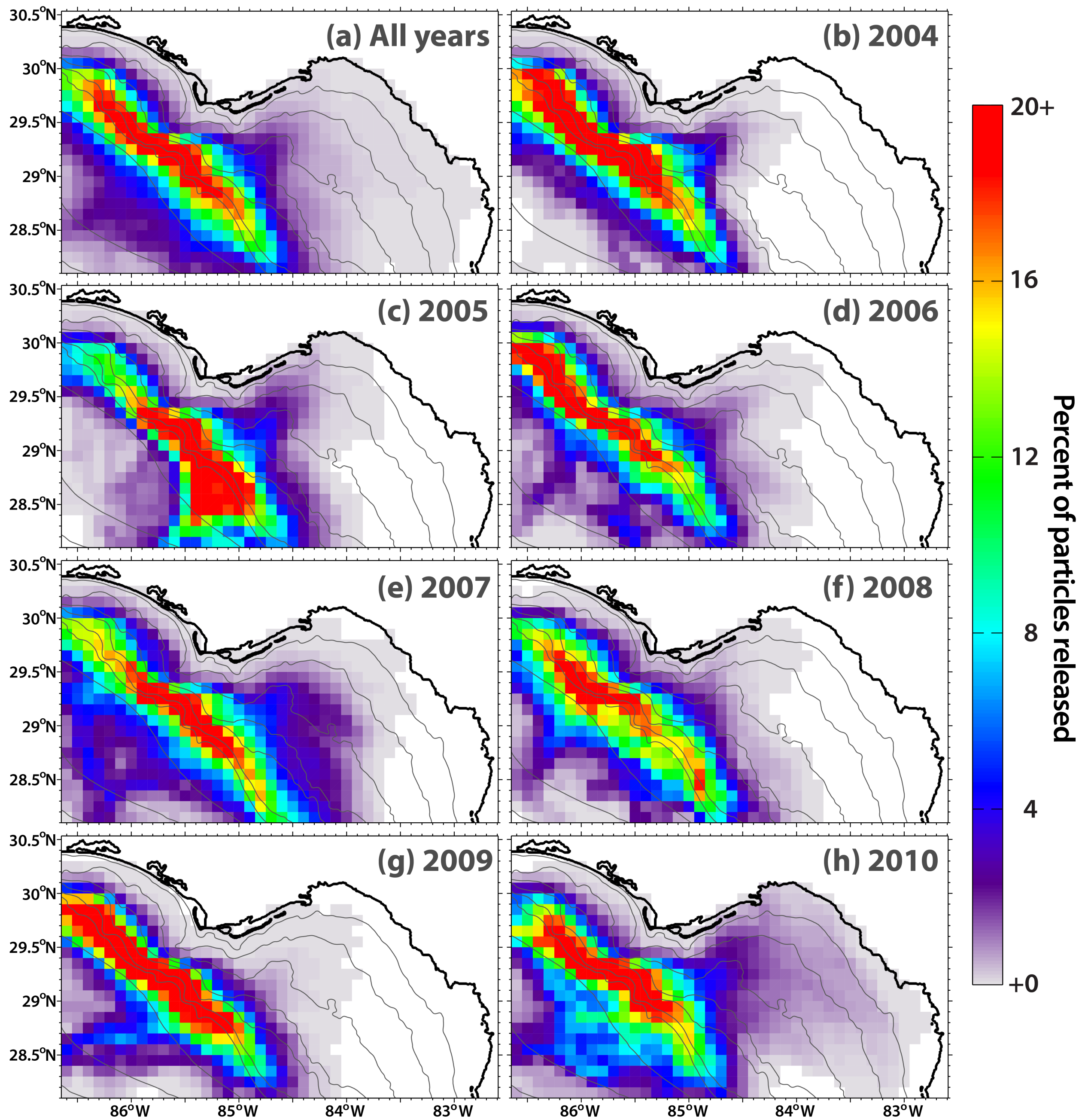

Figure 18: Particle track density for (a) all particles released over the seven-year advection period (percentage of all 733,824 particles), and (b)—(h) calculated for each year (percentage of 104,832 particles released during that year). Particles are advected in the depth-averaged velocities from the CFSR-forced BBROMS simulation.

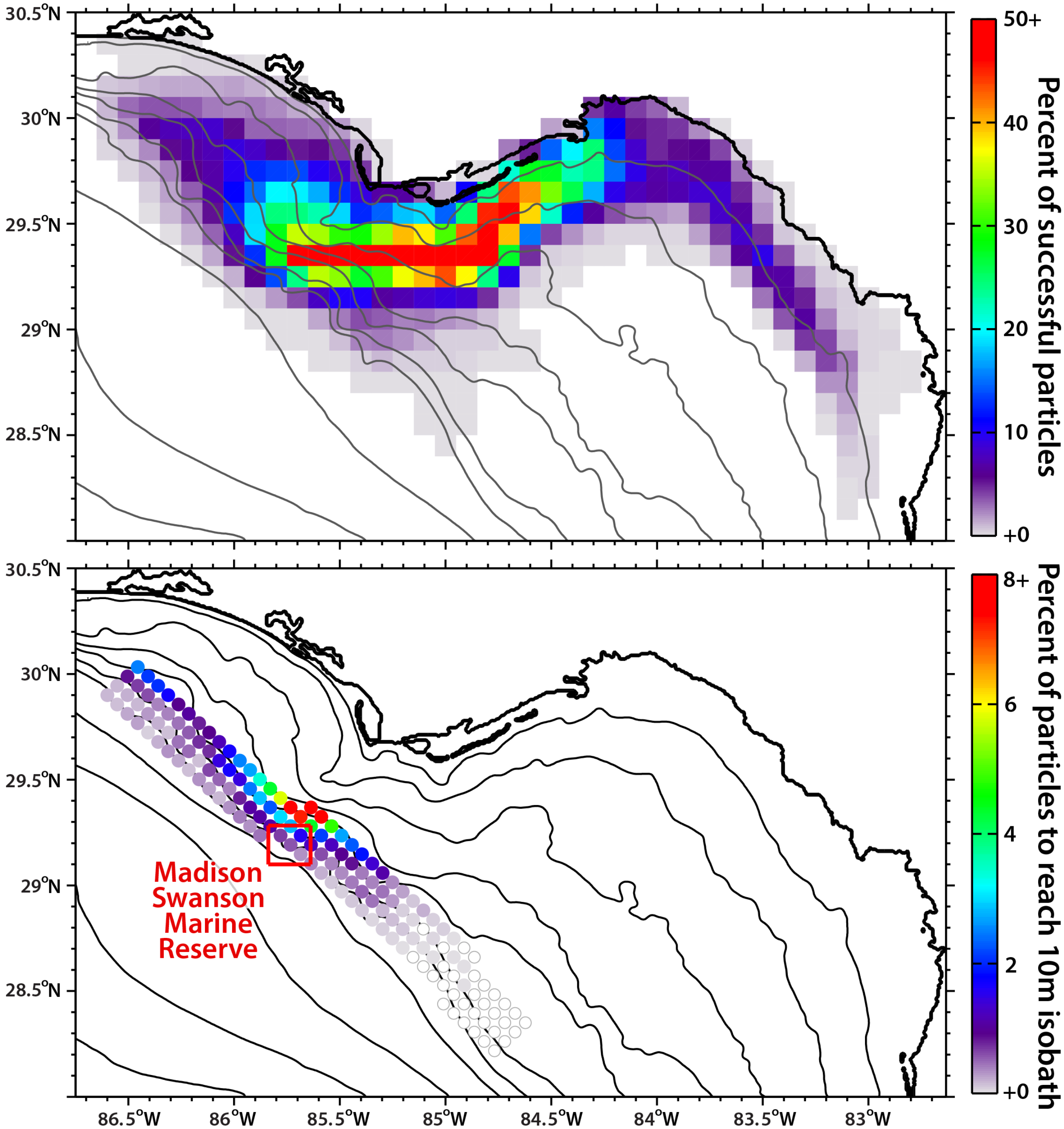

Figure 19: (top) Particle track density of all particles that reached the 10m isobath during their advection period and (bottom) the origins of particles that successfully reached the 10m isobath during their advection. Circles are colored by the percentage of successful particles originating from that location, where open circles indicate zero particles to arrive inshore.

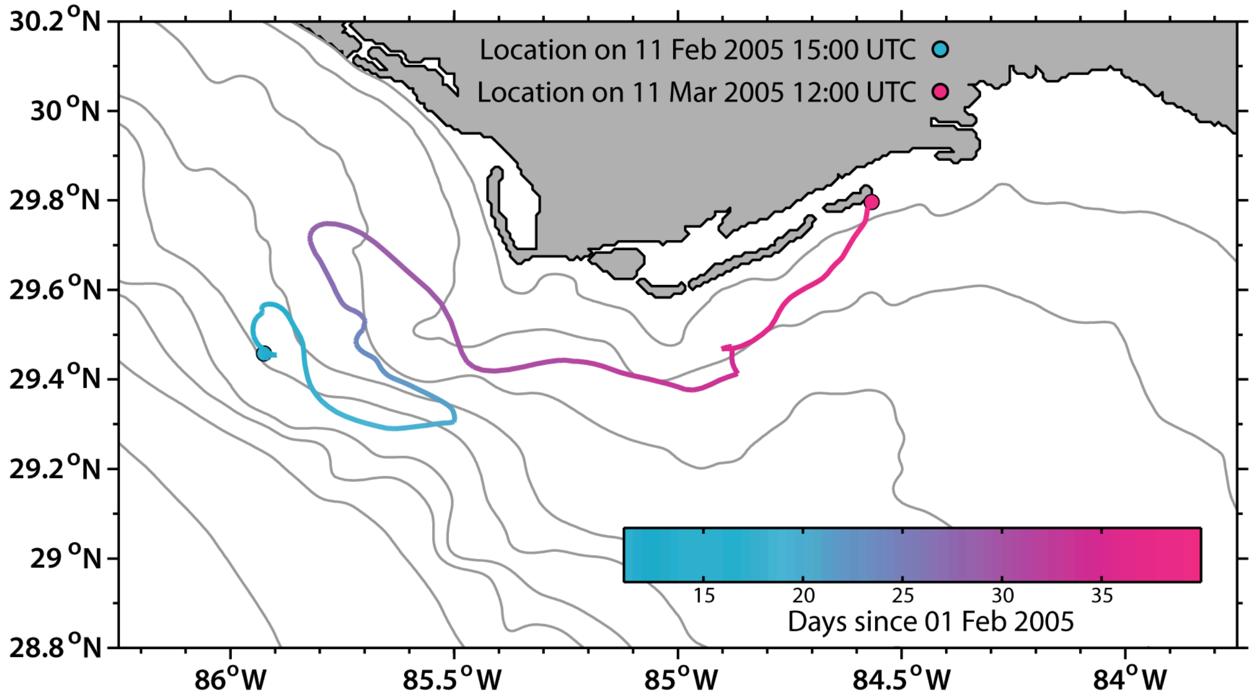

Figure 20: Trajectory of a particle released at 15:00 UTC on 11 February 2005. The color of the particle's path indicates the time during the particle's advection to the nearshore region around Apalachicola Bay on 11 March 2005 at 12:00 UTC.